JOURNAL OF MATERIALS SCIENCE **37** (2002) 1715–1746

Review
Electron backscatter Kikuchi diffraction in the scanning electron microscope for crystallographic analysis

K. Z. BABA-KISHI
The Hong Kong Polytechnic University, Department of Applied Physics, Hung Hom, Kowloon, Hong Kong, People's Republic of China
E-mail: apakzbab@polyu.edu.hk

The technique of electron backscatter Kikuchi diffraction patterns (BKDPs) in the scanning electron microscope is reviewed. The paper focuses mainly on the crystallographic applications of the technique, including discussions on point group and space group determination and strain analysis. Orientation microscopy is discussed but not reviewed. The geometrical configurations of BKDPs are reviewed in detail and the relationship between BKDPs and the technique of electron channelling patterns (ECPs) is explored briefly. Essential crystallography is discussed and methods of analysis of BKDPs to extract crystallographic information are analyzed in detail. Some important characteristics of diffraction contrast in BKDPs are analyzed with respect to the geometry of the technique, the dynamical theory of electron diffraction and crystallographic applications. Examples of the use of theoretical contrast in pattern interpretation are provided. Anomalous effects in BKDPs are analyzed in detail and ways of identifying anomalous contrast in practice are discussed. BKDPs included in the paper are zincblende (ZnS), silicon, germanium, GaAs, chalcopyrite ($CuFeS_2$), $TaTe_4$ and $Er_2Ge_2O_7$.

1. Introduction

Topographic imaging of bulk crystal surfaces using secondary electrons is the most widely applied method in the scanning electron microscope (SEM). The use of energy dispersive X-ray microanalysis in conjunction with sophisticated topographical imaging facilities, automated texture analysis and phase identification routines now available in modern SEMs, enable one to elucidate compositional, morphological and crystallographic characteristics of bulk materials.

In addition to secondary electron imaging, there are the various specialized imaging techniques in the SEM for materials characterization [1]. They include low-voltage microscopy, electron beam induced current (EBIC), backscatter or Z-contrast imaging, cathodoluminescence (CL) and low-loss electrons imaging [2–4]. Electron diffraction techniques including electron channelling patterns (ECPs) [5], UHV reflection-high energy electron diffraction (RHEED) [6], scanning reflection electron microscopy (SREM) by diffuse scattering [7] and backscatter Kikuchi diffraction patterns (BKDPs) [8] have also been integrated into the SEM. Secondary electron imaging might be sufficient to yield the desired topographic information about a sample. However, to gain a better understanding of the crystal structure and texture [9, 10] of bulk crystals or thin films, it is often necessary to carry out detailed crystallographic and texture analyses of the specimen using BKDPs [11]. The detail and high contrast of BKDPs combined with wide angular range exceeding 90° across the diagonal, and high intrinsic spatial resolution make BKDPs suitable for crystallographic analysis. Phase identification by crystallographic point group or space group classification, orientation microscopy and evaluation of plastic and elastic strains are the primary applications of BKDPs. An example of a BKDP recorded from a crystal of zincblende (ZnS) at 40 kV is shown in Fig. 1. The pattern illustrates a complex arrangement of Kikuchi lines and bands that can be used for detailed crystallographic studies.

BKDPs are formed in the SEM when a stationary parallel beam of electrons is allowed to converge on the bulk sample whose surface is tilted at about 70° with respect to the primary electron beam. Consequently, greater intensity backscattered out of the surface is obtained from a sub-micron area of the sample. The depth-resolution of the technique is better than 50 nm. Depending on the electron probe size and the beam current used, this resolution can be further improved.

The subject of this review article is to discuss the various characteristics and properties of backscatter Kikuchi diffraction patterns in detail. The discussion presented focuses on the capabilities and limitations of BKDPs, providing analysis particularly suitable for

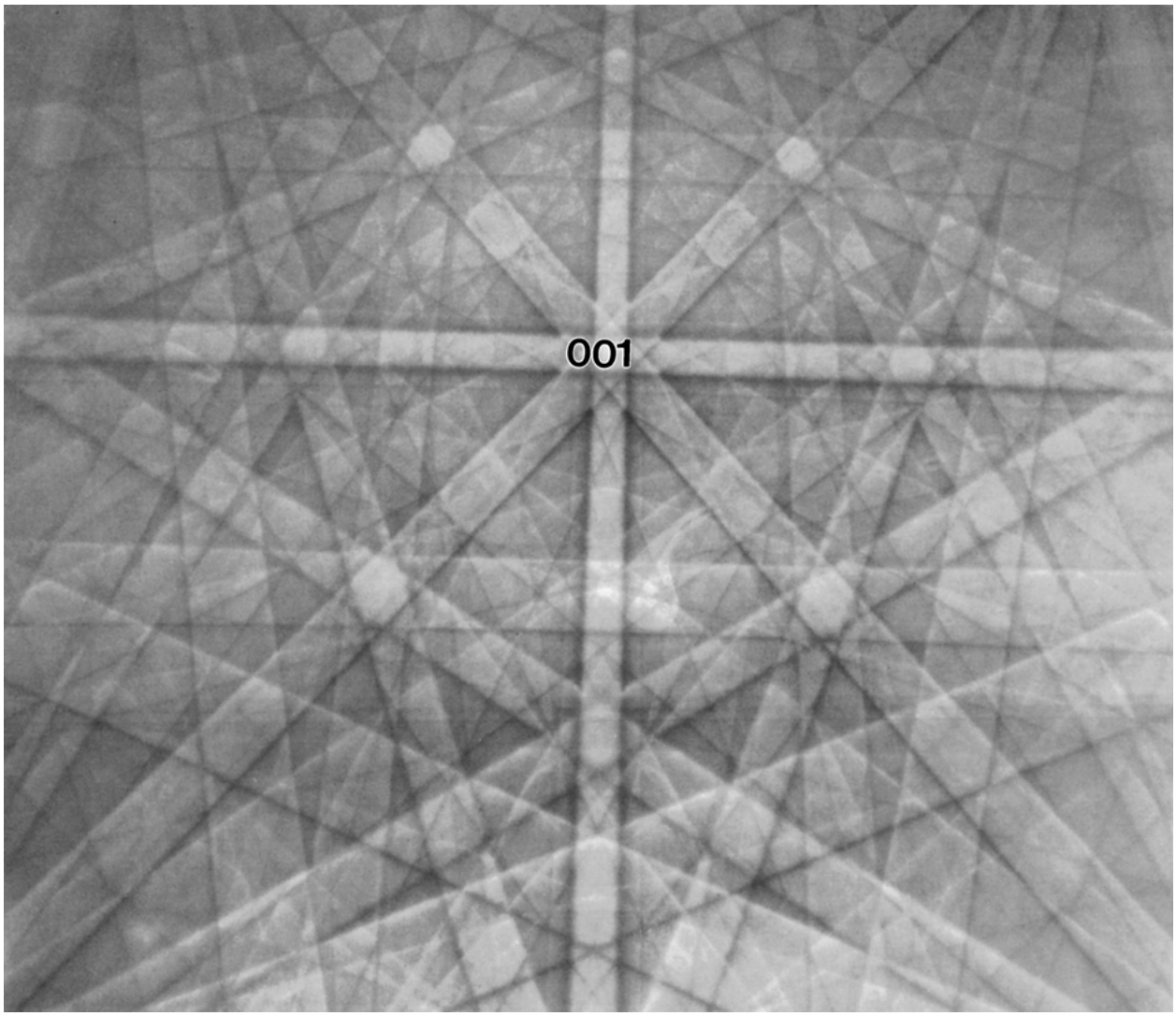

Figure 1 BKDP recorded from a crystal of ZnS or zincblende showing an extensive network of Kikuchi lines and bands that joint together at various projected zone axes. The symmetry of these Kikuchi bands can be used for phase identification, space group determination, micro-texture analysis and strain measurements. The [001] zone axis is marked.

crystallographic analysis. Texture analysis and orientation microscopy are discussed briefly, but the analytical and imaging aspects of the techniques are not reviewed in this article. The analysis of these techniques is extensive and requires a separate review article. However, a comprehensive list of references on texture analysis is provided.

2. Background

Kikuchi bands are the diffraction features that can be observed in the scanning electron microscope (SEM) by using the techniques of electron backscattering Kikuchi Patterns (BKDPs) [12], electron channelling patterns (ECPs) [5], and selected-area channelling patterns (SACPs) [13]. The bands seen on these patterns are the backscattered equivalent of Kikuchi bands that can be observed in the transmission electron microscope (TEM). Kikuchi obtained the first Kikuchi diffraction patterns in 1928, in studying the diffraction of electrons passing through a thin film of mica [14]. Kikuchi observed pairs of black and white lines, now called Kikuchi lines. Many workers who obtained Kikuchi lines in the reflection diffraction mode, Shinohara [15] and Boersch [16] followed the work of Kikuchi. Most of these early patterns showed diffraction details within only a few degrees from the incident electron beam. Kikuchi bands are now a common feature of diffraction patterns in modern TEMs, and can, for example, be useful for crystal orientation determination [17].

Large-angle electron backscatter Kikuchi diffraction patterns were first recorded by Alam *et al*. in 1954 [18]. Most of the early work recorded patterns at only a few degrees deviation from the incident beam. Patterns at larger angles were suggested by Boersch [16]. Alam *et al*. recorded patterns at much larger deviations from the primary beam [18]. They recorded Kikuchi diffraction patterns directly on electron sensitive films, placed close to the specimen. Alam *et al*. called the patterns, high-angle backscatter Kikuchi patterns. The patterns were generated using a specially constructed instrument that allowed the electron beam to strike a bulk sample, which was steeply oriented with respect to the electron beam. The instrument utilized a single lens to focus the electrons onto the specimen. Among the

subjects investigated by Alam *et al*. were: variation in the diffraction contrast as a function of change in angle between the beam and the specimen and the influence of take-off angles on pattern collection.

In 1967, Coates, studying a large crystal of GaAs in the SEM observed unusual bands of contrast superimposed on a normal topographic image [19]. The bands were seen to follow the orientation of the crystal as if rigidly fixed onto the crystal surface. Coates referred to the bands as "orientation dependent" patterns [19]. Coates patterns, also referred to as pseudo-Kikuchi or Kikuchi-like patterns, were re-named electron channelling patterns (ECPs) and qualitatively interpreted by Booker *et al*. [20]. To generate ECPs, the electron beam is allowed to rock across a large area of the sample surface. Rocking the beam creates numerous angles with respect to the surface normal, resulting in variations in the total backscattered intensity. This variation in intensity is then recorded using the normal imaging detectors in the SEM and can be processed and displayed. The intensity variations also result in Electron Channelling contrast, which are used to image sub-surface dislocations. An early account of crystalline contrast using Electron Channelling effect in a SEM equipped with a field-emission filament is described by Pitaval *et al*. [21]. Electron Channelling contrast has also been used by Czernuszka *et al*. for imaging sub-surface dislocations [22]. A complete discussion of ECPs is beyond the scope of this paper. A review of ECPs and Electron Channelling contrast can be found in Wilkinson *et al*. [5]. Physical background of electron backscattering is analyzed in a review article by Niedrig [23].

The technique of ECP requires a very large and flat specimen. The selected area in an ECP is large, but its resolution can be improved by using a small divergence angle $<0.05^\circ$ at normal incidence. This however, has the disadvantage of reducing the angular range of the patterns. To overcome this, an important progress was made by Van Essen *et al*. who showed that ECPs could be generated by rocking the electron beam over a selected point on the specimen surface [24]. The SEM was modified in order to rock the electron beam over a fixed point on the surface. The resulting patterns were named selected-area channelling patterns (SACPs). The technique can be used to record diffraction patterns from individual crystallites in a ceramic material, providing a resolution of about 5 μm and an angular coverage about 15° [25, 13]. A comprehensive bibliography of SACPs is published by Joy and Newbury [26].

Venables *et al*. in 1973 [27] developed a technique in the SEM by placing a phosphor screen about 25 mm in diameter at a specimen-to-screen distance of about 10 mm. The size of the selected area was about 1 μm. The patterns recorded in this way were named electron backscattering patterns (EBSPs). Although patterns of this kind were recorded by Alam *et al*. in 1951 [18], Venables *et al*. [27] might have been unaware of this work. The observed backscattering intensities in EBSPs were weak due to low current densities on the phosphor. Some improvements were later made by placing a channel plate between the phosphor and the specimen, thus reducing the need for high beam current operations. The studies carried out by Venables and co-workers culminated in the application of EBSPs to micro-crystallography [28] and crystallographic orientation determination in the SEM [29]. Using a field emission SEM, Harland *et al*. demonstrated that diffraction patterns from regions about 50 nm apart could be recorded [30]. The technique of EBSP was shown to be a better and more versatile alternative to the familiar ECPs [31].

Following the work of Venables *et al*. [27], Dingley and co-workers at the University of Bristol, e.g., Worthington, Razavizadeh, and Lorretto attempted to improve the resolution of EBSPs by recording the patterns directly on photographic film. Preston in 1983 [32], improved and partially developed a camera for EBSPs, originally built by Razavizadeh, who used the camera for recording Micro-Kossel X-ray diffraction patterns [33]. Preston made important contributions to the development of EBSPs including an evaluation of their applicability to crystallographic problems. Further improvements in the camera design were carried out by Baba-Kishi in 1984, and methods were devised for systematic crystallographic analyses of diffraction patterns recorded from the seven crystal systems [34].

The acronym EBSP has been commonly used to describe the technique, particularly in orientation microscopy [35]. Electron backscattering diffraction patterns corresponding to the acronym EBSD is also in use [5, 36]. To differentiate EBSPs from backscatter imaging or Z-contrast imaging, and to represent it as a unique diffraction technique along the work of Alam *et al*. [18], the term backscatter Kikuchi diffraction (BKD) was adopted [8, 37]. The acronyms BKD, and BKDPs will be used throughout this article to describe the technique.

3. Geometry of BKDPs

Backscatter Kikuchi diffraction (BKD) is a real-space crystallography technique. The most convenient method of describing its geometry is by Frank's Construction [38]. Frank's Construction was originally developed to illustrate the geometry of Kossel diffraction patterns, but it is equally applicable to explain the geometry of BKDPs.

Frank's Construction involves two spheres: the Ewald sphere and the Fermi sphere, both radii $\frac{1}{\lambda}$, Fig. 2a. The Fermi sphere is drawn with its origin at the centre of the reciprocal space, O. The origin of the Ewald sphere, E, lies on the surface of the Fermi sphere. The condition for a reflection to occur is that the Ewald sphere must pass through both a reciprocal lattice point G, and the origin of the Fermi sphere, which coincides with the divergent source of electron radiation. As illustrated in Fig. 2a, the loci $OE_{\bar{G}}$ and $OE'_{\bar{G}}$, describe circles on the Fermi sphere. The circles also lie on Brillouin planes, which are the normal bisector planes of the reciprocal lattice points, for example, G and G′. Subsequent elastic scattering of the divergent electrons by a set of crystal planes, produces a double conic with a semi-angle $(\pi/2) - \theta_B$, where θ_B is the angle in the Bragg's equation $2d_{hkl} \sin\theta_B = n\lambda$, where λ is

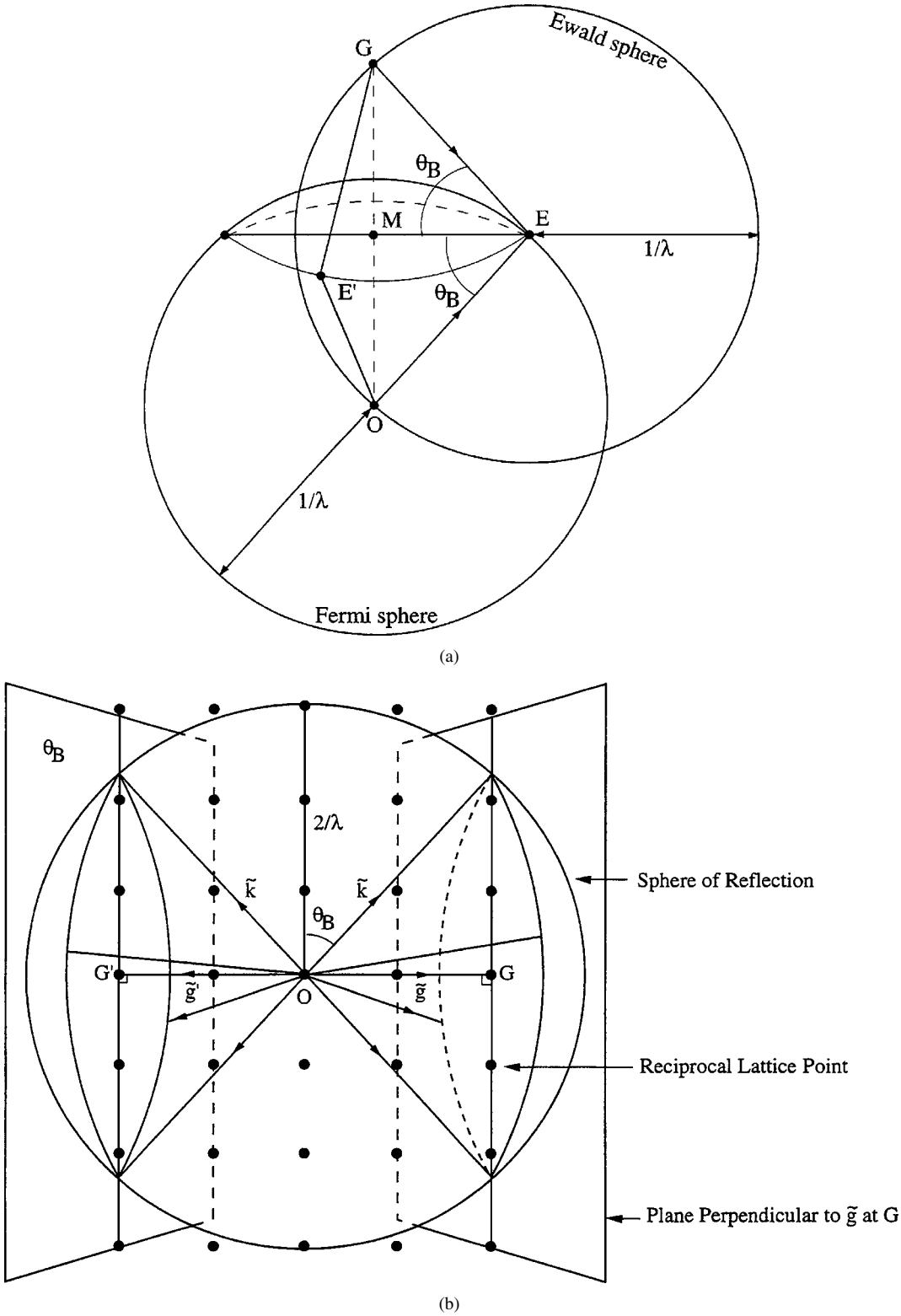

Figure 2 (a) Frank's model of the Ewald sphere and the X-ray Fermi sphere. This model can be used to generate cones of radiation in both X-ray Kossel and BKD patterns. The point O is the origin of the reciprocal space, E is the centre of the Ewald sphere, θ_β is the Bragg angle, M is the mid-point of OG and λis the wavelength. OG = 1/d; (b) Reciprocal lattice construction of the geometry of BKDPs using a sphere of reflection. G is the reciprocal lattice point, $\bar{g}$ is the reciprocal lattice vector and $\bar{K}$ is the wavevector.

the electron wavelength. From Fig. 2a, $\frac{1}{2d} = GM = GE \sin\theta_B = \frac{1}{\lambda}\sin\theta_B$. The line OG corresponds to $1/d$. It therefore follows that $2d \sin\theta_B = n\lambda$.

The geometry of BKDPs can also be described by constructing a sphere of reflection, radius $\frac{1}{\lambda}$, as shown in Fig. 2b. To generate a specific cone-pair, two planes, perpendicular to the reciprocal lattice vectors $\bar{g}$ and $\bar{g}'$, are drawn through the reciprocal lattice points G and G′, respectively [34]. The origin, O, of the sphere of reflection is the divergent electron source, which coincides with the origin of the reciprocal space. The intersections of the planes with the sphere of reflection are circles, which are joined to the origin by the wavevectors K. The wavevectors lie on cones with cone axes perpendicular to the diffracting crystal planes and are of semi-angle $(\pi/2) - \theta_B$.

A simple consideration in visualizing the geometry of Kikuchi lines is that a large set of cones generated by elastic scattering of electrons within the crystal planes are directed onto a flat recording plane in gnomonic projection. This recording plane is placed some distance away from the sample surface. BKD patterns formed in this way are therefore the records of specific sections of the cones. The intersections of these cones with the recording plane are, in fact, hyperbola but in practice they are approximated to straight-lines as illustrated in Fig. 3a and b. The arrays of cones generated represent the crystal symmetry in real-space and contain details of the structure factors [39, 40]. The number of Kikuchi lines or the number of double-cones of radiation on the recording plane, depends on the population of reciprocal lattice points within the sphere of reflection [34]. The number of diffracting reciprocal lattice points also depends on the radius of the sphere of reflection, which is determined by the wavelength λ of the electrons used. Using an incident beam of energy 30 kV, the wavelength of the inelastic source within the sample is approximately 0.07 Å. This indicates that θ_B in Fig. 2b is small and the resulting cones are therefore shallow.

4. BKDPs in gnomonic projection

BKDPs are recorded on photographic film or viewed on phosphor screen in gnomonic projection. Kikuchi lines and bands correspond to the intersections of the double cones of intensity with the recording screen positioned in the polar gnomonic [41]. The recording screen can be termed as gnomonogram, which is the plane tangential to the sphere at pole, P, Fig. 4a and b. The geometrical characteristics of BKDPs in polar gnomonic can be described as follows:

1. The polar point of the gnomonic corresponds to the pattern centre (PC), which is equivalent to the divergent electron source, originally positioned at the centre of the Fermi sphere or sphere of reflection.
2. Electrons scattered parallel to the equatorial line through the centre of the sphere, would appear at infinity.
3. The diffracting crystal is placed at the centre of the sphere, and the normal drawn to each facet of the crystal projects that facet onto the plane of projection. The point of intersection of the normal with the plane of projection is referred to as a pole.
4. The distance between any pole (zone axis) and the pattern centre is described by $r \times \tan(90 - \phi)$, where r is the perpendicular distance between the origin and the pattern centre.

Gnomonic projection provides patterns with co-linear zone axes. The normals drawn to a set of crystal planes located in one zone axis, lie on a single plane and intersect the plane of projection on straight zone-lines. The projection however, is not angle-true. This applies to both inter-plane and inter-zone angles. The angles that appear between zone-lines on the projection plane, do not correspond to the real interzone angles in the crystal. Also, plane traces are not angle-true except those that intersect within or close to the PC. The major problem inherent to gnomonic projection is the progressive distortion in the pattern, as the distance between the PC and the projected poles increase. Consequently, the most useful crystallographic information is located within the proximity of the PC.

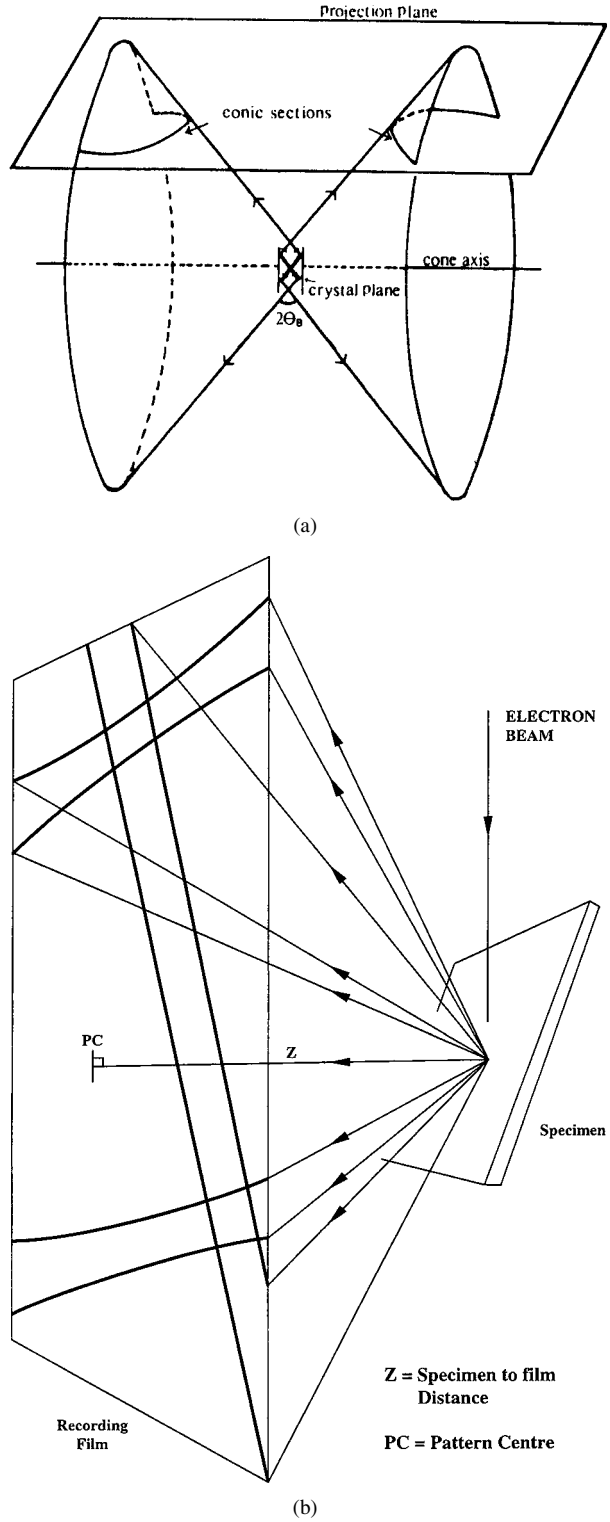

Figure 3 (a) Geometrical representation showing the hyperbolic intersections of a double cone of electron radiation with the recording plane in gnomonic projection; (b) Diagram showing the intersections of double cones of radiation with a flat recording plane in gnomonic projection as approximately straight lines. The pattern centre on the recording plane is equivalent to the electron source point within the specimen. Re-drawn from A. Preston [32].

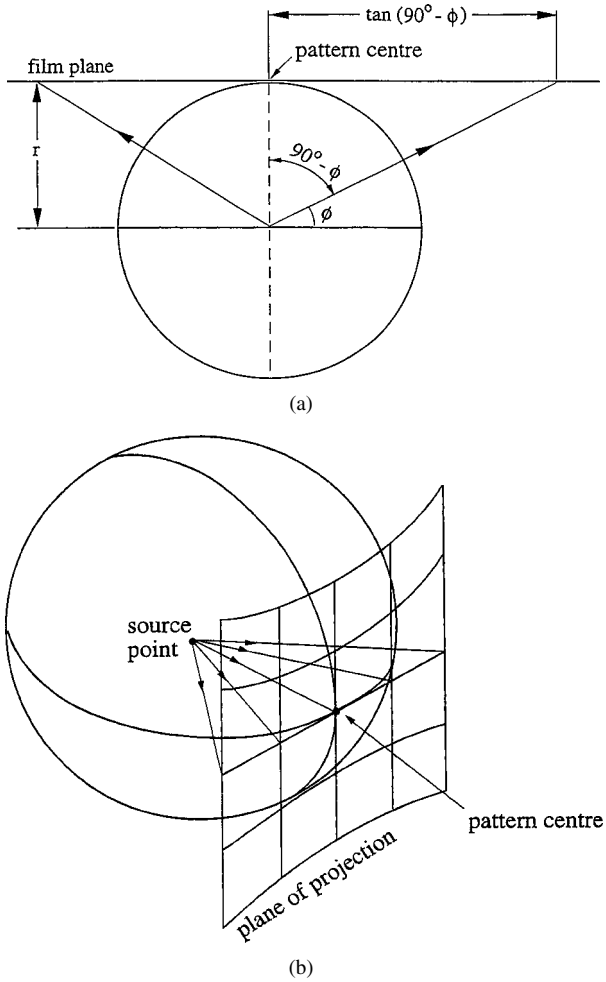

Figure 4 (a) Geometrical characteristics of polar gnomonic projection. The pattern centre in a BKDP corresponds to the pole of the gnomonic projection; (b) Distortion in the plane of projection introduced by polar gnomonic projection.

5. Pattern centre

Pattern centre (PC) is the most important parameter that needs to be identified on the pattern before any other measurements can be carried out. There are three methods for determination of (PC) on BKDPs: the Pitsch method, the three-ball method and the known-orientation method.

The Pitsch method was originally developed by Halbig *et al*. [42] to find the PC on Kossel patterns. Worthington and Vaudin in their studies at the University of Bristol, have independently described variations to the Pitsch method for use on BKDPs (Unpublished Ph.D. work). The three-ball method was developed by Biggin *et al*. [43] for Kossel patterns and was used by Venables and Bin-Jaya [44]. This method is particularly suitable for Kossel patterns, which are mostly used for precise measurement of lattice parameters [45]. BKDPs do not provide the precision of the X-ray Kossel patterns, and therefore, the use of a lengthy three-ball method is unnecessary in BKDPs. The Pitsch method is very sensitive to measurement errors, but has the advantage that the PC can be determined from a single recorded pattern and without a need for other calibration information.

The known-orientation method is extensively used for determination of PC on BKDPs for both crystal texture and crystallographic applications [46, 47]. The principle involves recording a calibration BKDP from a specimen with a known crystallographic orientation with respect to the primary beam and the recording plane, Fig. 5a. The calibration specimen such as a cleaved (001) silicon or germanium single crystal wafer is oriented such that a specific zone axis is projected as a perpendicular to the recording plane. Two examples of calibration patterns are shown in Fig. 5b and c, which were recorded directly on film and phosphor screen, respectively. The accuracy of the known orientation method is estimated to be 1°. A more detailed discussion of the known-orientation method and modifications to this technique can be found in Randle [47] and Baba-Kishi [48].

Once the position of PC is determined, various other measurements are carried out on the calibration pattern. The pattern centre can be extrapolated onto a pattern recorded from another specimen for crystallographic analysis. The measurements that can be performed include, specimen-to-film-distance, inter-planar, inter-zonal and Bragg angles. The geometrical characteristics of these measurements are extensive, and the reader is referred to Baba-Kishi for detail [48].

6. Experimental aspects of BKDPs

6.1. Microscope operation and BKDP detection

To obtain a BKDP, the specimen is oriented such that its surface-normal subtends an angle 65°–75° with the incoming primary electron beam. The specimen surface is first studied using the secondary electron imaging facility and a region of interest is selected. The scanning coils are then switched off so that the electron beam can be positioned as a stationary probe on the point of interest in the selected region of the specimen surface, Fig. 6a. The BKDP formed is viewed on a phosphor screen, Fig. 5c, and then recorded by inserting an electron microscope photographic film into the specimen chamber, Fig. 6b. Alternatively, the BKDP is viewed using a sensitive CCD camera, and the resulting image is retrieved by a computer for on-line processing. This method is commonly used in orientation microscopy and automated or manual texture analysis.

Pattern centre can also be determined by setting the objective lens current at a constant value, while the working distance is fixed. Moving-camera calibration can therefore be carried out at a various values of the objective lens currents, eliminating the need for the working distance read-out. This methods of pattern-centre determination improves accuracy, but is mostly applicable to flat samples. The added precision of the moving-camera method could also prove useful in lattice parameter determination, assuming the BKDP can be fully indexed. A set of three high-index Kikuchi likes can be selected for this purpose.

To record a BKDP on phosphor screen, suitable for subsequent retrieval into a computer memory, an image intensifying television camera with a maximum gain of 10^5 can be used. The camera is positioned outside the SEM chamber so as to focus on the phosphor screen through a lead-glass window as illustrated in Fig. 6b.

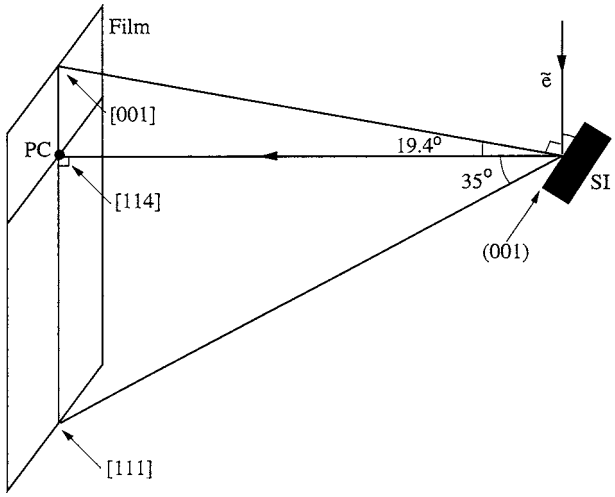

(a)

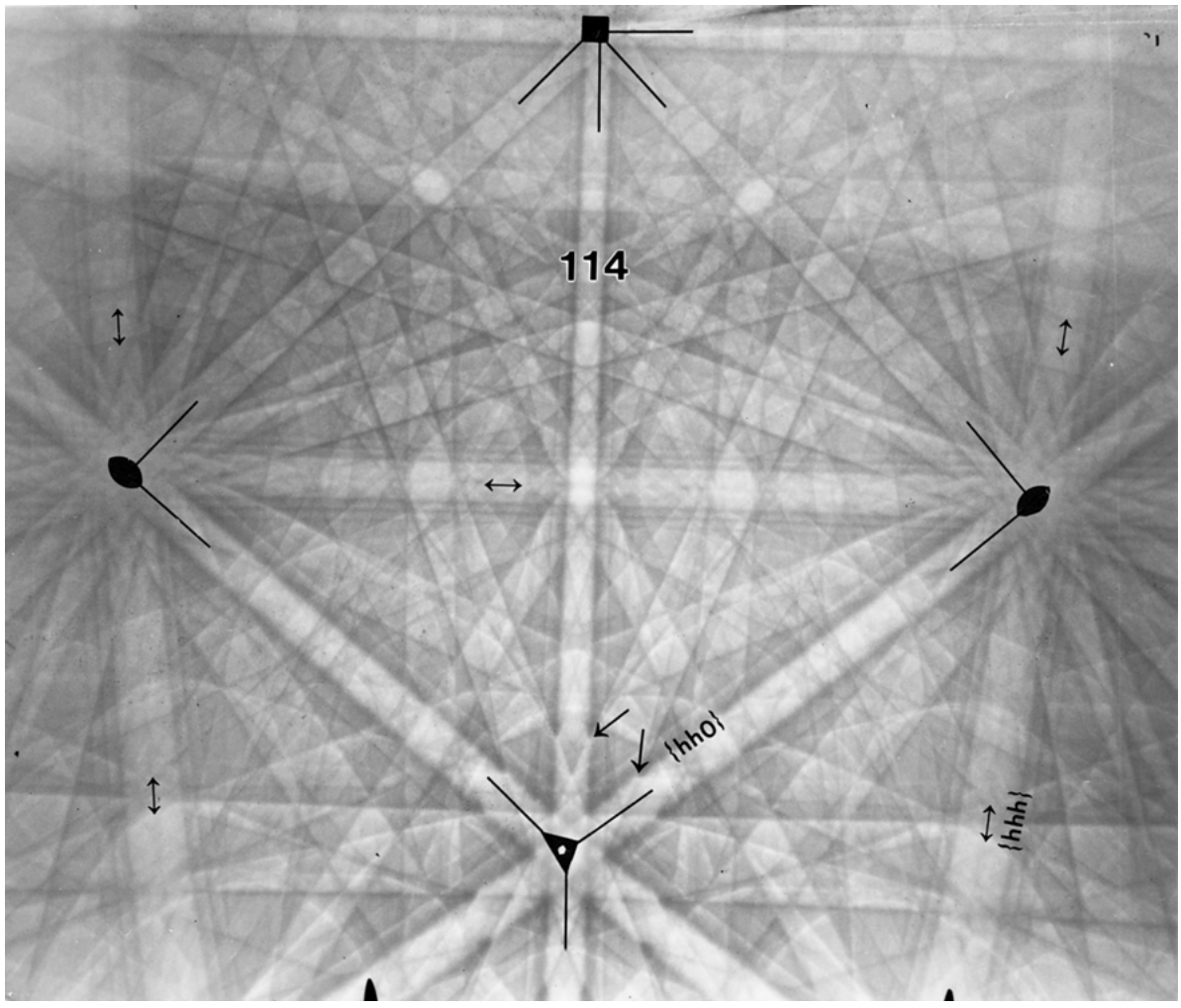

(b)

Figure 5 (a) The geometry of the known-orientation method for determination of PC. The zone axis [114] corresponds to the pattern centre, and lies vertically above the [111] zone axis; (b) BKDP recorded on film from a cleaved (001) crystal of silicon at 40kV. The zone axis [114] is the pattern centre, where there is no observable distortion due to gnomonic projection; (c) BKDP recorded on phosphor from a cleaved (001) crystal of silicon under the same conditions as in Fig. 5b. (*Continued.*)

The purpose of the lead glass is to prevent X-rays from leaving the SEM chamber. In conjunction with this, a temporal filter and an image-integrator can reduce the probe current to $\sim 10^{-11}$ amps, allowing diffraction patterns from sub-10 nm particles to be recorded. It is now customary to use low-cost CCD cameras together with an image integrator to achieve results similar to that of the earlier image intensifying cameras.

To obtain a BKDP for various crystallographic analyses [12, 49–52], or for elastic and plastic measurements [53, 54], it is best to record them on photographic film. The resolution of an electron microscope film is superior to that of an image collected by a CCD camera. A BKDP recorded on film can also be enlarged to a useful level so as to assist with symmetry inspection or with measurement purposes. A film camera originally

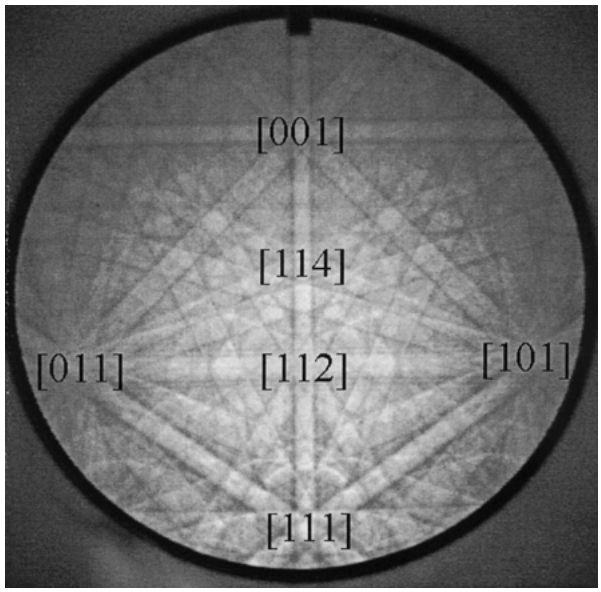

(c)

Figure 5 (*Continued.*)

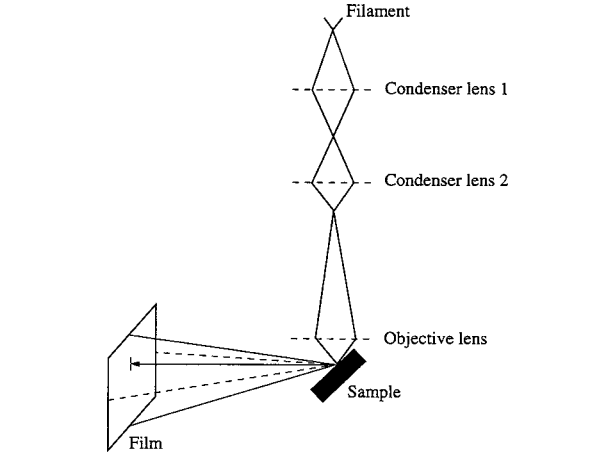

(a)

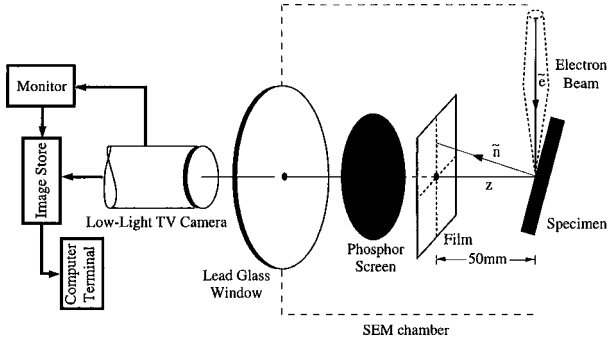

(b)

Figure 6 (a) Simple ray diagram illustrating the mode of operation of the SEM for recording BKDPs which are obtained using the spot-mode of the SEM; (b) Experimental set up for recording BKDPs. To record BKDPs, an electron microscope film can be placed inside the SEM chamber. Alternatively, BKDPs can be viewed through a phosphor screen and recorded using a CCD camera, placed outside the chamber. Such a pattern can then be used for microtexture analysis.

designed by Worthington (unpublished Ph.D. work) at Bristol University for recording X-ray Kossel diffraction lines, was successfully modified by Razavizadeh [33], Preston [32] and Baba-Kishi [12] to record BKDPs routinely. The camera operated in the vacuum, and incorporated a mechanism to enable insertion of ten consecutive electron microscope films into the chamber.

6.2. Resolution

The resolution of BKDPs is anisotropic and could vary according to the microscope operating conditions. Based on the studies carried out by Hjelen and Nes [55], the resolution is influenced by a variety of microscope conditions. These conditions include the working distance, specimen angle of tilt with respect to the primary beam, probe current and the accelerating voltage. At high accelerating voltages, e.g. 30 kV, the lateral resolution is reduced because of the increase in the penetration depth of the primary electrons within the specimen. Using a phosphor screen to display and subsequently store a diffraction pattern in the computer memory, there must exist sufficient diffracted electron flux in order to penetrate the outer aluminum coating of the phosphor. The lowest primary electron energy required for penetrating the aluminum coating of the phosphor screen is 20 kV. According to Hjelen *et al.* [55], the optimum lateral resolution obtained for an aluminum specimen at 70° tilt, is 660 nm and 250 nm, perpendicular and parallel to the tilt axis, respectively. The depth-resolution of the diffraction volume is considerably better than the lateral resolution and is estimated at 50 nm for aluminum studied at 20 kV.

Both the lateral and depth resolutions can be improved when, instead of a phosphor screen, a recording film is used. The electron flux intensity required to record a diffraction pattern on film is by an order of magnitude lower than that required to observe a diffraction pattern on phosphor screen. Consequently, probe current can be reduced, resulting in a reduction in beam diameter. The use of photographic film can therefore indirectly lead to an improvement in both the lateral and depth resolutions by about 50%.

The primary electron beam voltage combined with the characteristics of the specimen, for example, atomic number, limit the spatial resolution of BKDPs to about 0.5 μm [56]. Consequently, fine-grain materials, especially those with heavy deformation are less suitable for characterization with BKDPs. Measured crystallographic textures are also limited to about 2°. Consequently, fine details of grain boundaries and grain misorientations can not be studied by BKDPs. This limitation of BKDPs is well demonstrated by Farstad *et al.* [57], showing better resolution along the specimen tilt axis compared with resolution perpendicular to the tilt axis. A characteristic of BKDPs that limits resolution and leads to substantial image foreshortening is the steep angle of tilt of the specimen. The reported measured resolution is 23–120 nm along the tilt axis and 50–200 nm perpendicular to the tilt axis. These values show improvement over the values measured using an aluminum specimen [55]. The dependence of spatial resolution on primary electron beam voltage and mean atomic number, has been investigated by Patterson *et al.* [58]. Using specimens of Al, Cu, and Ag, the range of measured spatial resolution is 0.9 μm at 40 kV

to 0.2 μm at 10 kV. One needs to consider, however, that best BKDPs are recorded at about 20 kV or higher.

To study misorientation and grain boundary morphology, TEM analysis offers a superior resolution [17]. However, the volume of crystalline materials investigated by TEM is severely limited, thus is of poorer statistical value.

A study of fine-grained materials described by Humphreys *et al*. shows the limits of BKDP resolution [59]. According to this study, the angular resolution using LaB6 filament is 200–500 nm. The effective spatial resolution using conventional filament is about 50–150 nm parallel to the tilt axis and 150–500 nm perpendicular to the tilt axis. This shows the resolution limit for fine-grained materials or sub-grains. A method of measuring effective spatial resolution is also described in this study. The required spatial resolution for analysis of 1mm grains is 100 nm perpendicular to the specimen tilt axis and about 30 nm parallel to the tilt axis. A resolution of 30 nm is not attainable in a conventional SEM. In studying fine-grained structures, measured intercept grain size is therefore overestimated. Optimization of spatial resolution is also discussed in this study. Preliminary study of resolution in a field emission SEM is also reported, indicating an improvement of about 10 times over resolution in a conventional SEM.

6.3. The influence of microscope parameters on BKDPs

The conditions that affect the quality of BKDPs can be summarized as follows:

1. By a change in electron beam current carried out by adjusting condenser lenses, the contrast and spatial resolution of BKDPs can be changed. An increase in probe current increases the probe diameter. This results in greater beam spread, which increases the background contrast and thus reduces the spatial resolution.

2. A change in the value of the accelerating voltage causes a change in the angular width $2\theta_B$ of Kikuchi bands—the wider the bands, the easier they are to analyze. This change in the angular width originates from a change in the wavelength of the electrons, which reduces or increases the diameter of the sphere of reflection, as described in Section 3.

3. The use of 30–40 kV generates high-quality BKDPs, providing extensive diffraction detail. Although Kikuchi lines can be obtained at low voltages, the practical requirement for BKDPs is about 20 kV. This is because the phosphor screen is most efficient at 20 kV or above. The level of both the electron microscope film and camera sensitivity to low diffraction intensities also imposes a restriction on pattern visibility.

4. Representative SEM values for on-line camera imaging are about 30–40 kV operating voltage, 1 nA beam current and 40 nm probe current. For recording BKDPs directly on photographic film, representative SEM settings are: 10–40 KV, 0.5 nA beam current, 10–20 nm probe current and 2–10 seconds film exposure. These values could vary depending on the type of microscope, film and camera used.

6.4. Specimen preparation, charging and surface contamination

Preparation of specimens for BKDP studies is relatively simple. For crystallographic analysis, most samples can be fractured or cleaved, which produce the highest quality patterns. Cleaning the sample by ultrasound in a solution of Methanol, assists in recording good quality patterns. This method however, can not be readily applied to certain thin films or metallic interlayers, since surface damage might result. For microtexture studies of alloys and ceramics, reasonably large and flat samples are needed. To expose grain boundaries, surface etching of the sample is also necessary. Prior to surface etching, it is essential to carry out careful lapping and polishing. Both should be carried out with care to minimize surface damage. BKDPs are sensitive to surface damage primarily because the penetration depth of the primary electrons is rather shallow, e.g., 1000 Å, for aluminum. Consequently, the escape distance of the scattered electrons is confined to this distance. The problems of the escape distance and the penetration depth of the primary electrons have been studied by Wells [60, 61]. The shallowness of the escape distance of the primary electrons is an important and useful property that has been used by Wells [62] and Baba-Kishi [7] for imaging of various surface features. It is therefore important to reduce surface damage, which causes incoherent scattering and leads to degradation of BKDPs.

An amorphous surface layer and surface contamination that degrade BKDP quality can be caused by a variety of factors. Surface exposure to the atmosphere, lapping, polishing, chemical etching and surface contamination as a result electron beam interaction with surface impurities, can all significantly reduce Kikuchi band sharpness and contribute to diffuse background contrast.

It has been found by the author that the highest quality BKDPs originate from samples that are fractured or cleaved immediately before they are transferred into the SEM chamber. Unsatisfactory BKDPs often originate from samples that are lapped and polished, particularly when the polish quality is low. When the amorphous layer is thick, in the order of 1000 Å, there is an appreciable initial retardation in the primary beam energy before entering into the crystalline layer. A certain proportional of the electrons that undergo anomalous absorption and scatter by crystal planes, are then rediffracted by the thick amorphous surface layer; this can lead to a significant loss of crystalline contrast. When the surface layer is $\sim$30 Å, the primary beam while retaining most of its initial energy, penetrates through the layer, but the coherence of the outgoing back-diffracted electrons is partially lost in the amorphous layer. This also leads to some degradation in BKDP contrast. Surface contamination about 10 Å thick, does not lead to appreciable pattern degradation, but can cause an increase in diffuse background contrast. In addition to initial surface contamination, a surface can easily degrade in the SEM during both the diffraction and imaging

modes. While surface contamination is not a serious problem in topographical studies, it can rapidly degrade the diffraction quality, particularly when the chamber vacuum is unsatisfactory.

Low level surface damage or contamination is not a serious problem in BKD studies, provided lapping and polishing are carried out with care, and the sample is transferred to either the SEM chamber for subsequent studies or stored in vacuum or kept in a solution of Methanol. Proper sample storage is particularly important when strain analysis is required. Samples that can be fractured or cleaved require no preparation. "As received" samples, especially thin films on substrates can be cleaned using a cleaning solution prior to investigation in the SEM.

Non-metallic materials invariably store electrostatic electron charge as a result of the primary electron beam striking the sample surface. The degree of charging depends on the accelerating voltage, probe current and the sample size.

Two forms of specimen charging need to be considered in BKDP studies. One is charging of the entire specimen during topographic studies, and the other is the localized charging during diffraction studies. Insulating and to some extent, semi-insulating materials are unsuitable for microtexture analysis. This is particularly true when information about grain boundary geometry, grain misorientation and mesotexture analysis are required. Sample charging would simply prevent these from being studied. Coating the sample with a very thin layer of carbon would not prevent charging, and any increase in the thickness of the conductive layer would prevent the formation of a meaningful diffraction pattern.

One way of assessing the charging behaviour in a sample irradiated by a uniform scanning electron beam, is to consider the variations in the emission yield coefficient with respect to the primary beam voltage. The emission yield coefficient is defined as I_e/I_i where I_e and I_i are the emitted and incident currents, respectively [63]. The maximum emission yield coefficient for metals varies between 0.6 and 1.6 for a primary beam voltage ranging from 1 kV to 800 V. For semiconductors and insulators, this maximum yield coefficient varies between 1 to 20. For an insulator investigated at 30 kV, for example, the yield coefficient is well below the maximum value, leading to excessive charging and possible thermal damage to the specimen [63].

Coating the sample surface prevents charging effects, but inevitably leads to BKDP degradation or its loss. A variety of materials have been used to coat the surface, including carbon, gold, aluminum and titanium with little success [8]. The most effective method of reducing electrostatic charging is to use the smallest possible specimen in diffraction studies. For crystallographic and strain analyses, a specimen about 1 mm^2 is sufficient to yield BKDPs. The adverse effects of electrostatic charging can be further reduced by the use of silver paint around the edges of the sample. In orientation microscopy, relatively large specimens with flat surfaces are required. There is no effective method of reducing electrostatic charging. However, satisfactory patterns can be recorded by a combination of reducing the accelerating voltage and probe current, use of small objective aperture and by limiting the time of impact of the beam on the surface. Yamamoto [64] has investigated the influence of surface layer coating on the resulting diffraction patterns. The empirical results obtained by Yamamoto indicate that total deterioration of a diffraction pattern is possible when the thickness of the deposited surface layer is $1.5/\mu_0$. The mean absorption coefficient of the electrons for the deposited material is μ_0. According to Yamamoto, a 500 Å thick Al, or 200 Å thick Cr would result in total loss of diffraction at 20 kV. For crystallographic and orientation analyses by BKDPs, sharp and undistorted diffraction patterns are required. A preliminary study indicates that a surface layer of carbon, 20–50 Å thick, leads to significant loss of diffraction quality [45]. For most applications, therefore, surface coating would lead to unsatisfactory diffraction patterns.

Diffraction patterns are obtained, when the electron beam is stationary and focussed onto a specific position on the sample. In non-conducting materials, the stationary beam leads to localize charging, creating a complex charged environment that results in the distortion of the electron beam. A brief account is given here, which is due to Thong [65].

In localized irradiation, two forms of charging occur. One is positive charging of the irradiated core, and the other is negative charging of the region very close to the irradiated core. Positive charging results in the emission yield coefficient being larger than unity, and consequently creates retarding field. This retarding field is the catalyst for the attraction of some low-energy secondary electrons onto the surface where the retarding field is present. These secondary electrons tend to reduce the retarding effects of the positive core field, thus reducing the emission yield coefficient. However, it is unlikely that the environment becomes totally neutral. It is thought that the equilibrium effects of negative charging are only temporary.

Experience by the author shows that reasonable BKDPs are attainable for a short period after the beam impact on the surface. If the beam is allowed to remain on the surface, charging leads to noticeable distortion in the diffraction pattern. The secondary electron initiated negative charge creates a retarding field above the impact core and becomes significant with time. Indeed, experience shows that the electron beam does not drift away from the impact point immediately after the impact. Certain amount of time is needed for the drift to take place. The time needed for the beam drift depends on the specimen and the microscope operating conditions.

7. Backscatter Kikuchi diffraction pattern contrast

The contrast in BKDPs is governed by (a) the geometrical characteristics of the patterns, and (b) the crystalline contrast.

7.1. Geometrical characteristics of contrast

Electron backscatter Kikuchi diffraction patterns are the records of specific double-cones of intensities in

real-space. Sets of reciprocal lattice points generate specific sets of cones. These cones, depending on the orientation of the diffracting crystal planes, are either enhanced or weakened in intensities. In addition to structure factor considerations, the number of conics is limited by the electron wavelength of the diffracting source, the smaller the wavelength, the larger the radius of the sphere of reflection.

The contrast and visibility of BKDPs are essentially governed by

(a) the intrinsic scattering processes that take place within the interaction volume, and
(b) the geometrical characteristics of the recording technique in the gnomonic projection.

The geometrical constraints of the gnomonic projection result in a background intensity that varies across a BKDP; the centre of the pattern is significantly brighter than the edges. Since BKDPs are formed by a stationary point source within the sample, and the resulting diffraction patterns are projected onto a flat film, there is inevitably a distribution of intensity across the pattern. This distribution becomes non-uniform because the signal backscattered out of the surface has a non-uniform flux over the entire solid angle of the scattered electrons.

Signal/noise is a major consideration in BKDPs. To obtain a diffraction pattern with sufficient signal, it is necessary to use a primary beam of sufficient probe current, and at a minimum accelerating voltage 20 kV. Noise becomes a serious problem once the accelerating voltage is reduced below 20 kV, although BKDPs can be recorded at 10 kV. The problem of signal to noise ratio can be dramatically compounded when an insulator or semi-insulator specimen of low atomic number is investigated.

The distribution of background intensity in BKDPs is anisotropic. In a tilted specimen, the electrons that scatter out of a surface are asymmetrical and confined to a forward lobe, Fig. 7a. The electrons scattered out of a tilted surface strike the central region of the pattern at right angles, whereas they are incident on the edges at an oblique angle. Consequently, variations in intensity distribution result. The situation is shown in Fig. 7b, which illustrates a decrease in the number of electron intensity per unit area as a function of $\frac{1}{\mathrm{Cos}^3\phi}$. The angle ϕ is subtended between the source point, S, pattern centre C and the point P, which is a point some distance from C [32]. Assuming a uniform backscattered initial flux, the number of electrons within the projected areas A1 and A2 at C, and P are $\pi(l\delta\theta)^2$ and $\pi(l\delta\theta)^2/(\cos\phi\cos^2\phi)$, respectively. Unlike the projected area A1 at C, the projected area A3 at P is not circular; for a circular projected area at P, the number of electrons is approximately $\pi(l\delta\theta)^2/\cos\phi^2$.

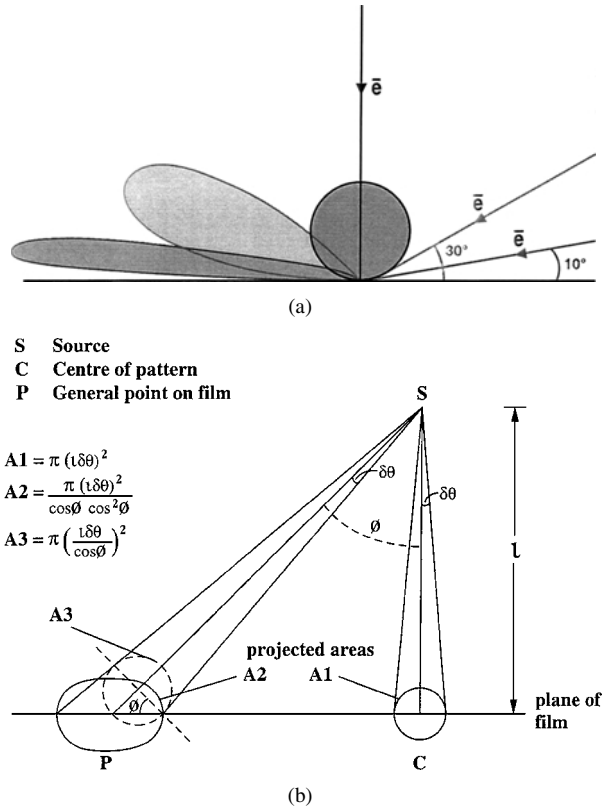

Figure 7 (a) Angular distribution of forward scattered electrons shown as function of the angle of tilt. The primary electron beam striking the sample vertically, creates symmetrical distribution of the scattered electrons, which follow the cosine rule. To obtain BKDPs, the primary beam strikes the sample at an oblique incidence, scattering the electrons in the forward direction; (b) Diagram illustrating large-angle intensity variations in BKDPs. The centre of the pattern at C, is darker than the edges. Scattered electrons incident on the unit area of the phosphor or film decreases as $1/\mathrm{Cos}^3\phi$. Re-drawn from A. Preston [32].

7.2. The crystalline contrast

The main consideration in the dynamical theory is to determine wavefunctions in terms of linear combination of Bloch waves, which represent Eigen functions of wave propagation in the crystal. The approach is often simplified by the considerations that only one family of crystal planes diffracts the electrons. This happens by two pockets of electron waves of similar amplitudes close to the Bragg position; this is essentially the two-beam theory approach. The purpose of the various theories developed is to describe anomalous absorption by calculating electron wavefunctions and by determining the probably of their presence within crystal planes. The dynamical theory of electron diffraction describes anomalous absorption.

The contrast of Kikuchi lines in BKDPs can be explained by the use of kinematic theory in a similar manner to that used in transmission electron microscopy [66]. However, the contrast of Kikuchi bands can not be accounted for by the kinematic theory. Since BKDPs and ECPs are related by reciprocity, the theory of ECPs is valid for BKDPs. The intensity variations within the bands in ECPs have been calculated by Hirsch and Humphreys [67] by using the dynamical theory of electron diffraction. The variation of intensity within a band is based on the calculation by Joy [13] and Reimer [68].

To determine the wavefunction, a beam of electrons is viewed as a superposition of at least two Bloch waves within a crystal. The total backscattered intensity is then regarded as the sum of intensities from the excited Bloch waves for a certain angle of incidence. The

variations in the excitations of the Bloch waves, starting with the centre of the band where the angle of incidence is less than θ_B, and increasing to 2θ at the band edges, are then calculated. The theoretical intensities are sharper than the practical cases because the theory ignores energy losses, which lead to a range of possible θ_B, thus producing broader and less sharp band edges. The work of Sandstorm *et al*. [69] has taken certain aspects of energy losses into account, which has been used by Shorter and Dobson [70].

ECPs and BKDPs are generated by the process of anomalous absorption of electron waves within a crystalline sample [23, 71]. Anomalous absorption is a term used to describe fluctuations in the absorption of electron waves, when they travel in a direction close to the one that satisfies Bragg's law. The formal theory gives a complete account of the aspects mentioned above, is that due to Hirsch and Humphreys [72]. Reimer [68, 73], Vicario [74], Spencer *et al*. [75], Joy [13] and Booker *et al*. [76] have also given various other descriptions of this theory.

A useful aspect of the dynamical theory is the dispersion surface representation, which has been used to explain certain events in BKDPs. At the Bragg position which is coincident with the Brillouin zone boundary, the dispersion surface is separated by $\Delta K = \xi^{-1}$, where ξ^{-1} is the extinction distance in Fig. 8a. The dispersion surface is a pictorial description of the permitted waves, so that by representing on the diagram values of the Fourier coefficients Co and Cg, one can access immediately the prominence of a particular wave. The uses of such representations are shown in the text. For a complete discussion of the dynamical theory of electron diffraction, the reader is referred to Hirsch *et al*. [66]. The backscattering coefficients are evaluated using the phonon scattering theory of Hall and Hirsch [77]. The two-beam Hall and Hirsch theory is generalized to many-beam case in Spencer *et al*. [78]. This theory considers a Bloch wave in the crystal to be scattered into plane-waves. However, Humphreys and Hirsch [79] considered phonon scattering as the basic backscattering mechanism.

The expression for the backscattering coefficient has been modified by Spencer and Humphreys [78] and Priouz and Boswarva [80] in order to calculate the contrast across Kikuchi bands for tilted crystals. The geometry for a crystal surface tilted at a fixed angle to the undeflected beam is shown in Fig. 8b. The intensity of electrons associated with the Bloch waves, which are scattered out of the crystal, is a function of the backscattering coefficient, the crystal thickness and the amplitude of that Bloch wave at the crystal surface.

A quantitative analysis of ECP contrast has also been described by Dudarev *et al*. [81–83]. The theory accounts for large-angle scattering of electrons in Bloch states by thermal diffuse scattering. Subsequent multiple elastic and inelastic scattering of the electrons in Bloch states, which are excited by the incident primary beam, is described by an inhomogeneous transport equation. A supermatrix algorithm has been used by Dudarev *et al*. [81–83], to formulate a computational approach that allows simulations of multiple scattering of backscattered electrons in the crystal. In this way, the dependence of contrast on the detector position, and the energy of the backscattered electrons have been explained. An example of a pattern simulated using this approach is shown in Fig. 8c. The pattern shows contrast simulated at the primary incident electron energy 25 kV for the silicon (001) surface, using 200 beams. Using this approach, it has also been possible to simulate two-dimensional images of dislocations for various orientations of the Burgers vectors.

7.3. The reciprocity between ECPs and BKDPs

The theory given above was originally developed to explain contrast variations across Kikuchi bands in electron channelling patterns (ECP) [20, 66, 76]. Calculations carried out using expression (4) show that for normal incidence of electrons on the crystal surface, the Bragg scattered wavefields have a definite symmetry, with Kikuchi lines showing bright-dark contrast. Asymmetry is also observable experimentally and theoretically as pronounced "dark" (defect) lines on the low intensity side of the band and the "bright" (enhanced) lines on the high intensity side. In ECPs the asymmetry in Kikuchi lines increases with increasing angles of tilt.

BKDPs and ECPS are related by the theorem of reciprocity [27, 68, 84]. The following description on the reciprocity between ECPs and BKDPs is due to Reimer [84].

The geometrical relationship between BKDPs and ECPs is illustrated in Fig. 9. The reciprocity relationship between BKDPs and ECPs, based on their geometrical relationship, describes different points on BKDPs as being equivalent on ECPs. As illustrated, BKDPs are formed as a result of the angular distribution of a stationary beam of electrons, which backscatter out of the surface. ECPs are formed in a similar manner, except that rocking the electron beam on the crystal creates this angular distribution of the electrons. As a result, it can be assumed that the points of intensity contained within the angle ϕ_1, are reciprocally related to the points of intensity within ϕ_2, created by the variation of the rocking beam in ECPs, Fig. 9. Consequently, the solid angle of collection on the scintillator in ECPs is similar to the electron probe aperture in BKDPs. As a result, the angles ϕ_1 and ϕ_2, and α_1 and α_2 are equivalent, and thus reciprocally related. In both cases, the patterns generated are essentially due to the same scattering mechanisms of elastic and inelastic scattering. The theories developed for ECPs can in principle, be applied to explain contrast in BKDPs. Reimer [68, 84] has studied the reversal of contrast in Kikuchi lines from excess to defect in both ECPs and BKDPs. These studies show good agreement between the contrast observed in ECPs and BKDPs, thus confirming the reciprocity relationship between them.

8. Symmetry determination

The resolution and high-contrast provided by BKDPs, particularly those recorded directly on photographic film, enable crystallographic point group (CPG) to be

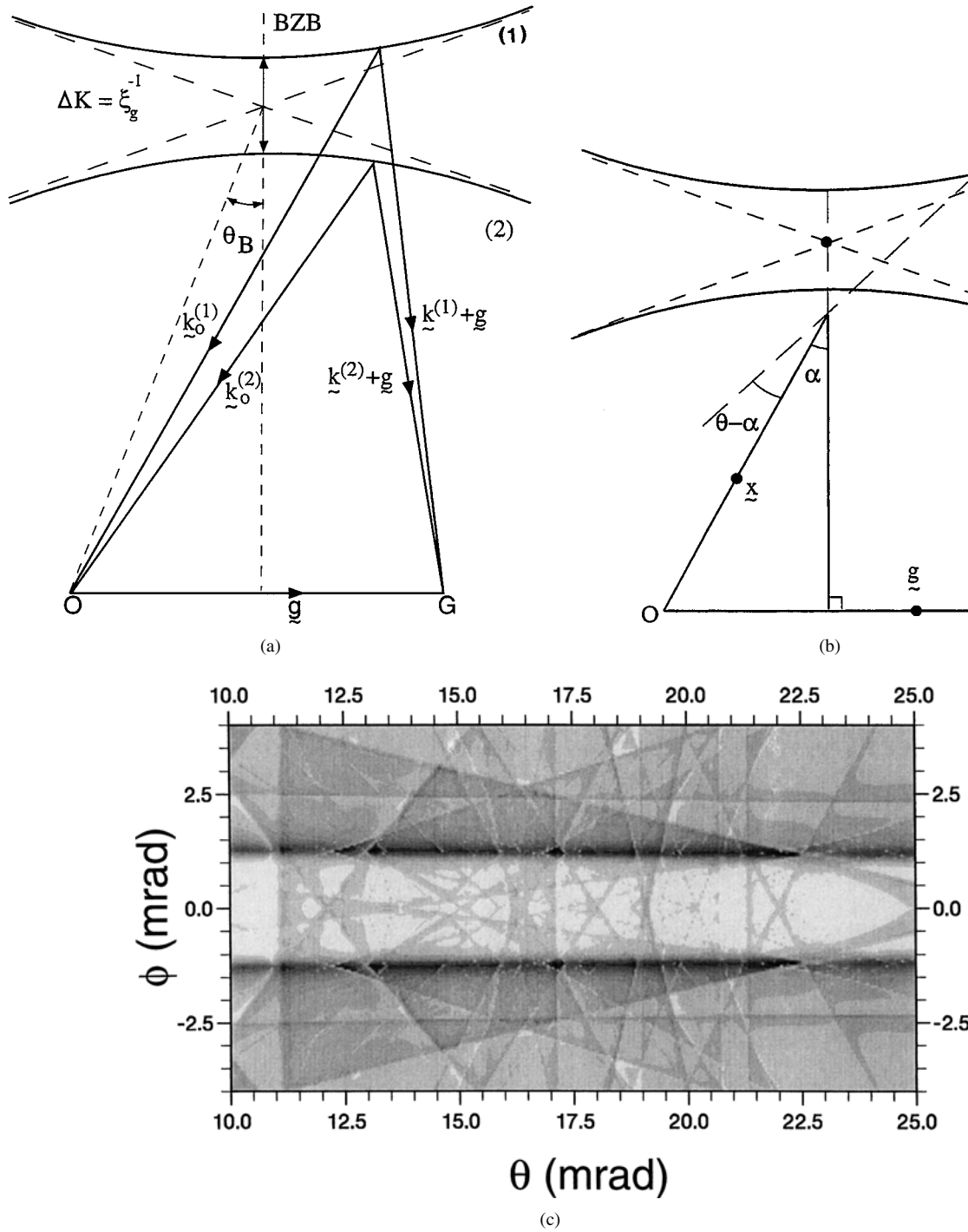

Figure 8 (a) The two-beam dispersion surface describes the waves excited in the crystal. The excitation points are separated into two parts on the Brillouin Zone boundary (BZB). This separation represents the inverse of the extinction distance ξ_g. The two branches (1) & (2) of the dispersion surfaces are marked; (b) The geometry in the reciprocal space for tilted crystals. $\underset{\sim}{\chi}$ is the incident wavevector and $\underset{\sim}{n}$ is a vector parallel to the crystal surface normal. G being the reciprocal lattice point, and $\underset{\sim}{g}$ a reciprocal lattice vector; (c) Electron channelling pattern simulated for silicon (001) surface using the density matrix approach. Courtesy of Sergei Dudarev.

determined. To carry this out, some knowledge of crystallographic principles particularly relevant to BKDPs is necessary. These principles are briefly described here.

An n-fold rotation axis is an imaginary line about which a motif is rotated through $(2\pi/n)$, producing a motif at a position indistinguishable from the initial position. The value of n is limited to 1, 2, 3, 4 and 6. A one-fold rotation axis (monad) signifies asymmetry, whereas 2-(diad), 3-(triad), 4-(tetrad) and 6-(hexad) fold rotation axes transform the crystal to self-coincidence. A rotation axis can be operated with or without inversion. An inversion symmetry axis is a distinct operation which combines a rotation through $(2\pi/n)$ about the axis, followed by an inversion through the centre of symmetry. A one-fold rota-inversion axis $\bar{2}$ describes centrosymmetry and combines the rotation of 360° with an inversion through the centre; thus generating a centre of symmetry. The $\bar{2}$ symmetry operation is equivalent to a mirror plane normal to the axis. Similarly, a six-fold rota-inversion $\bar{6}$ is equivalent to the combined operation of a three-fold rotation axis and a perpendicular mirror plane $(3/m)$. In general,

TABLE I Development of thirty-two possible non-identical crystallographic point groups shown as a function of increasing rotational symmetry operations

	Increasing rotational symmetry ⟶					
Rotation axis only	1	2	3	4		6
Rotainversion axis only	$\bar{1}$	$\bar{2}(\equiv m)$	$\bar{3}$	$\bar{4}$		$\bar{6}(\equiv 3/m)$
Combination of rotation axes		222	32	422		622
One rotation with perpendicular mirrors		$2/m$	$3/m\ (\equiv\bar{6})$	4/m		$6/m$
One rotation with parallel mirrors		$2mm$	$3m$	$4mm$		$6mm$
Rotainversion with rotation and mirrors			$\bar{3}2/m$	$\bar{4}2/m$		$\bar{6}2m$
Three rotation axes and perpendicular mirrors		$2/m\ 2/m\ 2/m$		$4/m\ 2/m\ 2/m$		$6/m\ 2/m\ 2/m$
Additional symmetry combinations present in Isometric (cubic) patterns		23	$2/m\ \bar{3}$	432	$\bar{4}3/m$	$4/m, \bar{3}2/m$

TABLE II The seven crystals system and the crystallographic point groups associated with each system. The essential symmetry operations required to generate the point groups in each crystal system are shown

Crystal system	Unit-cell shape	Essential symmetry	Point groups
Triclinic	$a\neq b\neq c;\ \alpha\neq\beta\neq\gamma$	One monad axis	$1, \bar{1}$
Monoclinic	$a\neq b\neq c;\ \alpha=\gamma=90^\circ\neq\beta,\ \beta>90^\circ$	One diad axix ($\|\|\ y$)	$2, \bar{2}(\equiv m), 2/m$
Orthorhombic	$a\neq b\neq c;\ \alpha=\beta=\gamma=90^\circ$	Three mutually perpendicular diads ($\|\|\ x$, y and z)	$222, mm2, mmm$
Trigonal	$a=b=c;\ \alpha=\beta=\gamma<120^\circ, \neq 90^\circ$	One triad ($\|\|[111]$)	$3, \bar{3}, 32, 3m, \bar{3}m$
Hexagonal	$a=b=c;\ \alpha=\beta=90^\circ,\ \gamma=120^\circ$	One hexad ($\|\|\ z$)	$6, \bar{6}, 6/m, 622, 6mm, 6m2, 6/mmm$
Tetragonal	$a=b\neq c;\ \alpha=\beta=\gamma=90^\circ$	One tetrad ($\|\|\ z$)	$4, \bar{4}, 4/m, 422, 4mm, \bar{4}2m, 4/mmm$
Cubic	$a=b=c;\ \alpha=\beta=\gamma=90^\circ$	Four triads ($\|\|\ \langle 111\rangle$)	$23, 2/m\bar{3}, 432, \bar{4}3m, 4/m\ \bar{3}2/m$

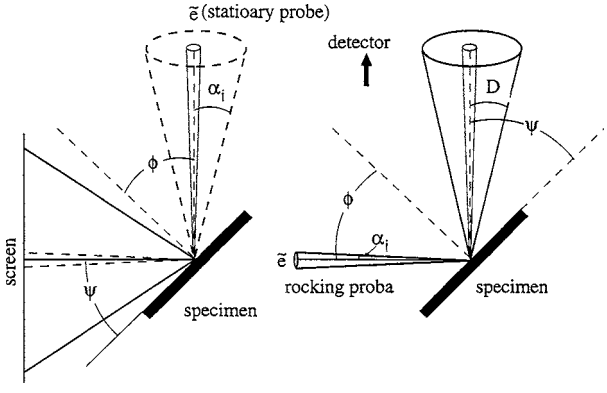

Figure 9 Diagrams illustrating the geometrical relationship between BKDPs (left) and ECPs (right). To show the reciprocity between the two techniques, the geometry of ECPs is rotated by 90° with respect to the primary incident electron beam.

the combined operation in three dimensions of rotation, inversion and reflection symmetry elements lead to 32 possible non-identical arrangements. These are called point groups. The development of the various point groups with respect to increasing rotational symmetries is shown in Table I. The method of interpretation of these symmetry operations in the seven-crystal system is shown in Table II, which is reproduced from Dana's Manual of Mineralogy [85].

As an example, consider the point group $4/mm$ ($4/m\ 2/m\ 2/m$) which is found in the crystals of whitetin (Sn) and Zircon ($ZrSiO_4$). This point group is represented by a four-fold rotation axis parallel to [001]. A mirror plane is perpendicular to [001], two mirror planes are perpendicular to both sets of ⟨100⟩, and ⟨110⟩ diads as illustrated in the stereograms in Fig. 10, which are due to Nye [86]. The distinct combination of the above features, by definition, signifies the most symmetric of the tetragonal structures. A similar approach is also adopted for the remaining six point groups of the tetragonal lattice. The point group $4/m$, for example, will feature a four-fold rotation axis with a mirror plane perpendicular to this axis, Fig. 10. A set of BKDPs taken from a crystal with the point group 422 will exhibit [001] as a four-fold rotation axis, while ⟨100⟩ are ⟨110⟩) will be featured as two-fold rotation diads with no mirror planes.

So far we have restricted the discussion of symmetry elements to point groups which consist of rotational axes, inversion axes and reflection planes. The nature of these symmetry elements is such that their operations lead to repetition of the original positions. The space group symmetry operations however, yield positions entirely different from the initial positions by means of translational symmetry operations. It is by virtue of such translational operations that a, b, c, n and d glide

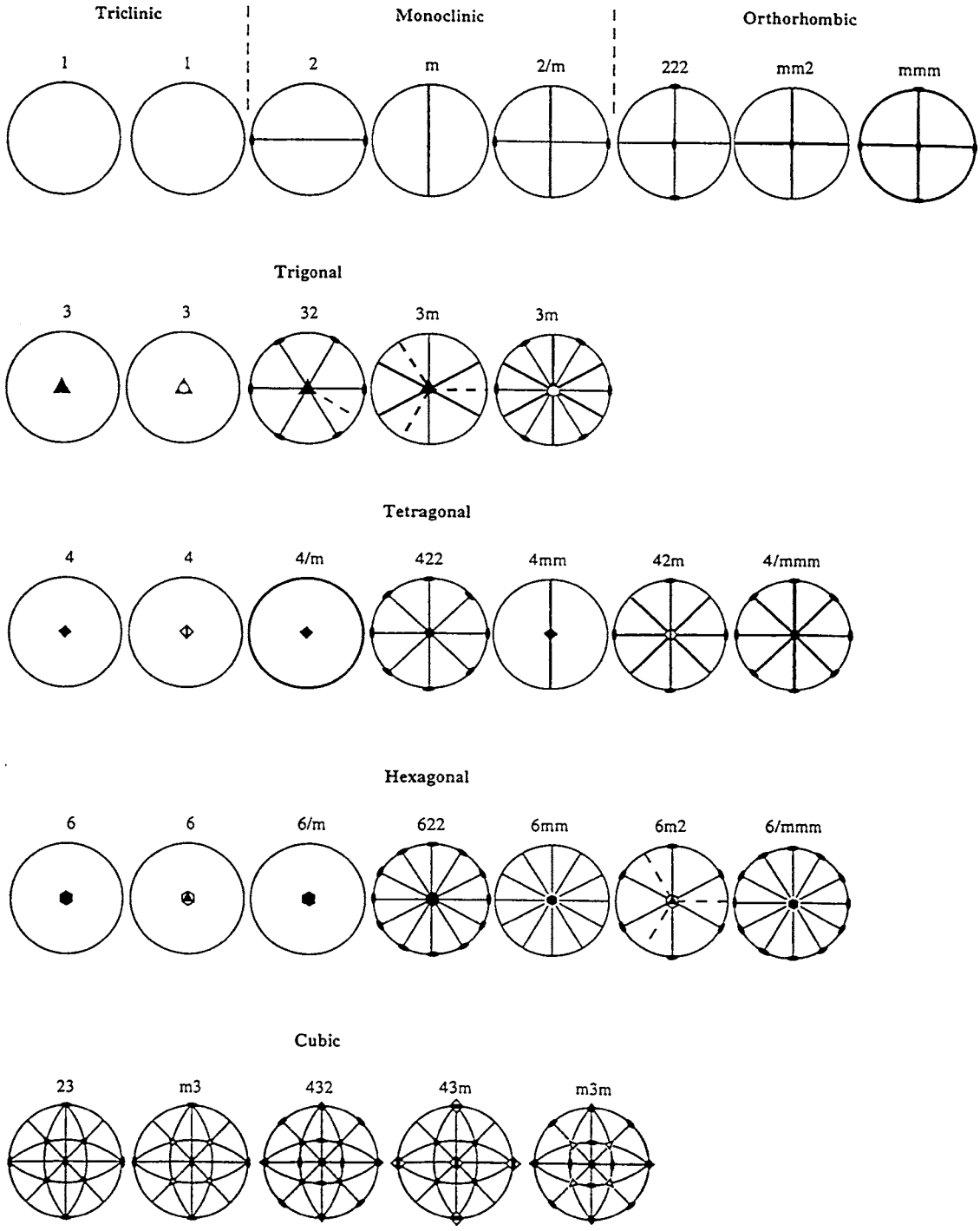

Figure 10 Stereographic projections showing the point groups for each of the seven crystal systems. Each projection shows the Laue group associated with a specific zone axis. These Laue groups can be combined to generate a whole-pattern three-dimensional point group. The relationships between the Laue groups, and zone axes in different crystal systems are also illustrated in Table V. The projections are re-drawn from Nye [86].

planes and the various screw axes are generated. The existence of these symmetry operations eventually leads to systematic absences of certain planes, a knowledge of which forms the basis of deriving space group symmetry in BKDPs. The analytical treatment of the nature of translational symmetry operations is discussed comprehensively by many authors [87–90]. It is appropriate however to discuss briefly the nature of screw axes, and glide planes.

The presence of a screw axis is conditional on the translation of an atom or a group of atoms parallel to the given zone axis by an amount 1/2, 1/3, 1/4, or 1/6 of the unit cell dimensions. For an n-fold screw axis, it is necessary to rotate the atoms or a group of atoms by $2\pi/n$ followed by an appropriate translation along the axis. A translational operation associated with a specific screw axis is always operated in the direction accepted by convention. For example, in a 4_1 screw axis, a rotation of $2\pi/4$ is followed by translation of 1/4 along the axis in the clockwise direction. In a 4_3 screw axis, a rotation $2\pi/4$ is followed by a translation in the anti clockwise direction and so on.

The influence of any screw operation on BKDPs, just as in TEM and X-ray patterns, is to extinguish a certain number of reflections. According to the Table III, a 4_1 screw axis extinguishes all reflections from planes

TABLE III Systematic absences of reflections due to screw axes

Orientation (in [ ] direction)	Translation component	Screw axis symbol	Class of reflection	Conditions for reflection
100	$a/2$	$2_1, 4_2$	$h00$	$h=2n$
100	$a/4$	$4_1, 4_3$	$h00$	$h=4n$
010	$b/2$	$2_1, 4_2$	$0k0$	$k=2n$
010	$b/4$	$4_1, 4_3$	$0k0$	$k=4n$
001	$c/2$	$2_1, 4_2$	$00l$	$l=2n$
001	$c/4$	$4_1, 4_3$	$00l$	$l=4n$
110	$a/2+b/2$	2_1	$hh0$	$h=2n$
0001	$c/2$	6_3	$000l$	$l=2n$
0001	$c/3$	$3_1, 3_2, 6_2, 6_4$	$000l$	$l=3n$
0001	$c/6$	$6_1, 6_5$	$000l$	$l=6n$

TABLE IV Systematic absences of reflections due to glide planes

Orientation (in ( ) planes)	Translation component	Glide plane symbol	Class of reflection	Condition for reflection
(100)	$b/2$	b	$0kl$	$k=2n$
(100)	$c/2$	c	$0kl$	$l=2n$
(010)	$a/2$	a	$h0l$	$h=2n$
(010)	$c/2$	c	$h0l$	$l=2n$
(001)	$a/2$	a	$hk0$	$h=2n$
(001)	$b/2$	b	$hk0$	$k=2n$
$(1\bar{1}0)$	$c/2$	c	hhl	$l=2n$
$(1\bar{1}00)$	$c/2$	c	$hh\,2hl$	$l=2n$
$(11\bar{2}0)$	$c/2$	c	$hh0l$	$l=2n$
(100)	$b/2+c/2$	n	$0kl$	$k+l=2n$
(010)	$a/2+c/2$	n	$h0l$	$h+l=2n$
(001)	$a/2+b/2$	n	$hk0$	$h+k=2n$
$(1\bar{1}0)$	$a/2+b/2+c/2$	n	hhl	$\begin{cases} 2h+l=2n \\ l=2n \end{cases}$
(100)	$b/4+c/4$	d	$0kl$	$\begin{cases} k+l=4n \\ k,l=2n \end{cases}$
(010)	$a/4+c/4$	d	$h0l$	$\begin{cases} h+l=4n \\ h,l=2n \end{cases}$
(001)	$a/4+b/4$	d	$hk0$	$\begin{cases} h+k=4n \\ h,k=2n \end{cases}$
$(1\bar{1}0)$	$a/4+b/4+c/4$	d	hhl	$2h+l=4n$

parallel to [001] except for $(00l)$ with $l=4n$, where n is an integer. Similarly a 2_1 screw axis extinguishes all planes parallel to [001] except for $(00l)$ with $l=2n$.

Glide planes are translational symmetry elements combining a plane of reflection with 1/2, or 1/4 of the lattice repeat translation along a direction parallel to the plane. The glide operation requires the presence of a mirror plane in the corresponding point group operation. A glide plane parallel to an edge of the unit cell, produces the axial glides a, b, and c. However, if the glide plane is along the unit cell diagonal, glides n and d are generated with their own specific translations as shown in Table IV. The table shows the systematic absences due to specific glide planes and glide directions. Systematic absences arising from the presence of screw axes and glide planes can be derived using structure factor expressions, in conjunction with appropriate translational symmetries. Details of these derivations can be found in references [87–89].

8.1. Crystallographic point group determination using BKDPs

Determination of an isometric (the most symmetric) point group is relatively straight forward, but as the symmetry decreases, this task becomes more difficult, see Table I. For a low symmetry crystal system, there is a minimum essential symmetry criterion and a set of BKDPs must exhibit this minimum symmetry in order to be able to yield a definite whole-crystal point group. In all cases, the extracted point group is one of the 32 point groups illustrated using stereograms in Fig. 10. Furthermore, the choice of crystallographic axes as outlined in Table II, must be consistent with the type of crystal symmetry.

To determine crystallographic point group, CPG using BKDPs, the essential consideration is to determine the crystallographic symmetries of various zone axes, i.e., the Laue point groups of low- or high- order zone axes. The Laue groups associated with each zone axis in various point groups are described in Table V. To carry this out, extensive visual examination of the patterns is required. Several diffraction patterns are often recorded from a crystal to include the zone axes needed for whole-crystal CPG determination. The number of diffraction patterns recorded depends on the crystal symmetry and specimen morphology. The patterns are inspected to identify the zone axes that are parallel to the crystal directions, x, y and z. The symmetry of a zone axis is identified by careful inspection of the symmetry characteristics of the Kikuchi lines that terminate in a zone axis [12, 49].

In determining CPG, the following details need to be noted:

1. The Laue groups belong to a subset of ten: $6mm$, $4mm$, $3mm$, $2mm$, m, 6, 4, 3, 2 and 1.

2. From the centrosymmetric crystal classes, the combinations of the ten Laue groups observed in BKDPs, allow identification of nine out of the eleven Laue classes with certainty: $2/m$, mmm, $4/m$, $4/mmm$, $3m$, $6/m$, $6/mmm$, $m3$ and $m3m$. This leaves out two Laue classes $\bar{3}$ and $\bar{4}$ as difficult cases to identify. To observe the diffraction symmetries of $\bar{3}$ and 3, it would also be necessary to record BKDPs with a minimum angular coverage of 180°. Triclinic point group $\bar{1}$ requires BKDPs with at least 360° coverage to allow possible identification of this point group or distinction between $\bar{1}$ and 1.

3. There are 21 non-centrosymmetric point groups of which 19 can be identified using BKDPs. They are 1, 2, m, 222, $mm2$, 4, 422, $4mm$, $42m$, 3, 32, $3m$, 6, 622, $6mm$, $62m$, 23, 432 and $43m$. The remaining rota-inversion point groups $\bar{4}$ and $\bar{6}$ are difficult to determine because the inversion axes have to observed. To achieve this, BKDPs covering about 360° would be required.

4. To determine the Laue group of a zone axis, decision has to be made about whether the projected diffracted symmetries of the BKDP allow a self-coincidence by reflection across a line or by rotation through an angle of 45°, 60°, 120° and 360°, or by rota-inversion. As illustrated in Table V, the number of individual Laue groups needed for identification of the whole-crystal CPG, depends on the crystal system. To illustrate this, BKDPs obtained from a crystal of germanium are analyzed.

TABLE V An illustration of the relationship between the various Laue groups and whole-pattern point groups. To determine a whole-pattern point group, it is essential to determine the Laue symmetry of an individual zone axis. The combinations of the various Laue groups yield the whole-pattern or three-dimensional point group

Point groups	Laue groups						
	⟨111⟩	⟨100⟩	⟨110⟩	⟨uv0⟩	⟨uuw⟩	[uvw]	
$m\bar{3}m$	3m	4mm	2mm	m	m	1	
$\bar{4}\bar{3}m$	3m	2mm	m	1	m	1	
432	3	4	2	1	1	1	
	⟨111⟩	⟨100⟩		⟨uv0⟩		[uvw]	
$m\bar{3}$	3	2mm		m		1	
23	3	2		1		1	
	[0001]	⟨11$\bar{2}$0⟩	⟨1$\bar{1}$00⟩	[uv.0]	[$uu.w$]	[$uu.w$]	[$uv.w$]
6/mmm	6mm	2mm	2mm	m	m	m	1
$\bar{6}m2$	3m	m	2mm	m	1	m	1
6mm	6mm	m	m	1	m	m	1
622	6	2	2	1	1	1	1
	[0001]			[uv.0]			[$uv.w$]
6/m	6			m			1
$\bar{6}$	3			1			1
6	6			1			1
	[0001]	⟨11$\bar{2}$0⟩			[$uu.w$]		[$uv.w$]
$\bar{3}m$	3m	2			m		1
3m	3m	1			m		1
32	3	2			1		1
	[0001]						[$uv.w$]
$\bar{3}$	3						1
3	3						1
	[001]	⟨100⟩	⟨110⟩	[u0w]	[uv0]	[$uu.w$]	[$uv.w$]
4/mmm	4mm	2mm	2mm	m	m	m	1
$\bar{4}2m$	2mm	2	m	1	1	m	1
4mm	4mm	m	m	m	1	m	1
422	4	2	2	1	1	1	1
	[001]				[uv0]		[uvw]
4/m	4				m		1
$\bar{4}$	2				1		1
4	4				1		1
	[001]	⟨100⟩		[u0w]			[uvw]
mmm	2mm	2mm		m	m		1
$mm2$	2mm	m		m	1		1
222	2	2		1	1		1
	[010]			[u0w]			[uvw]
2/m	2			m			1
m	1			m			1
2	2			1			1
							[uvw]
$\bar{1}$							1
1							1

8.2. Point group of germanium

Germanium has the isometric point group $m\bar{3}m$, indicating that the Laue groups 4mm (reflection tetrad), 3m (reflection triad) and 2mm (reflection diad) are required. The zone axes with Laue group 4mm, 3mm and 2mm can be indexed as [001], [111] and [110] respectively, with 4mm being parallel to the z-axis of the crystal.

The angular coverage of a BKDP is sufficient to record all the required symmetry elements of germanium on one pattern. However, several BKDPs are recorded so as to facilitate inspection. Fig. 11a, and b, illustrate the symmetries of the zone axes, [001], [111], marked T_1 and T_2, and [110], marked D_1, respectively. All the diffracted lines marked with solid lines have reflection symmetries and can therefore be brought into self-coincidence. Thus, the zone axes [001], [111] and [110] have individual Laue groups 4mm, 3mm and 2mm, respectively. The whole-crystal symmetry is therefore $m\bar{3}m$. It should be noted that we have not seen evidence on the pattern for the present of centre of symmetry. Direct observation of the centre of symmetry is, in fact, unnecessary in isometric crystals. The presence of 4mm, 3mm and 2mm imply that the centre of symmetry must be present in germanium.

8.3. Space group determination

Analogous with other diffraction techniques, e.g. convergent beam electron diffraction, BKDPs should be viewed as a complimentary crystallographic technique. Space group determination by BKDPs is possible, but might be time consuming and rather tedious, depending on the crystal system. BKDPs recorded from crystals that have known or partly known lattice parameters can be relatively easy to index. However, for unknown crystals, space group determination requires extensive measurements and an extensive series of computer simulations of the patterns. To carry out simulations, it is useful to have some idea of the Bravais lattice and/or

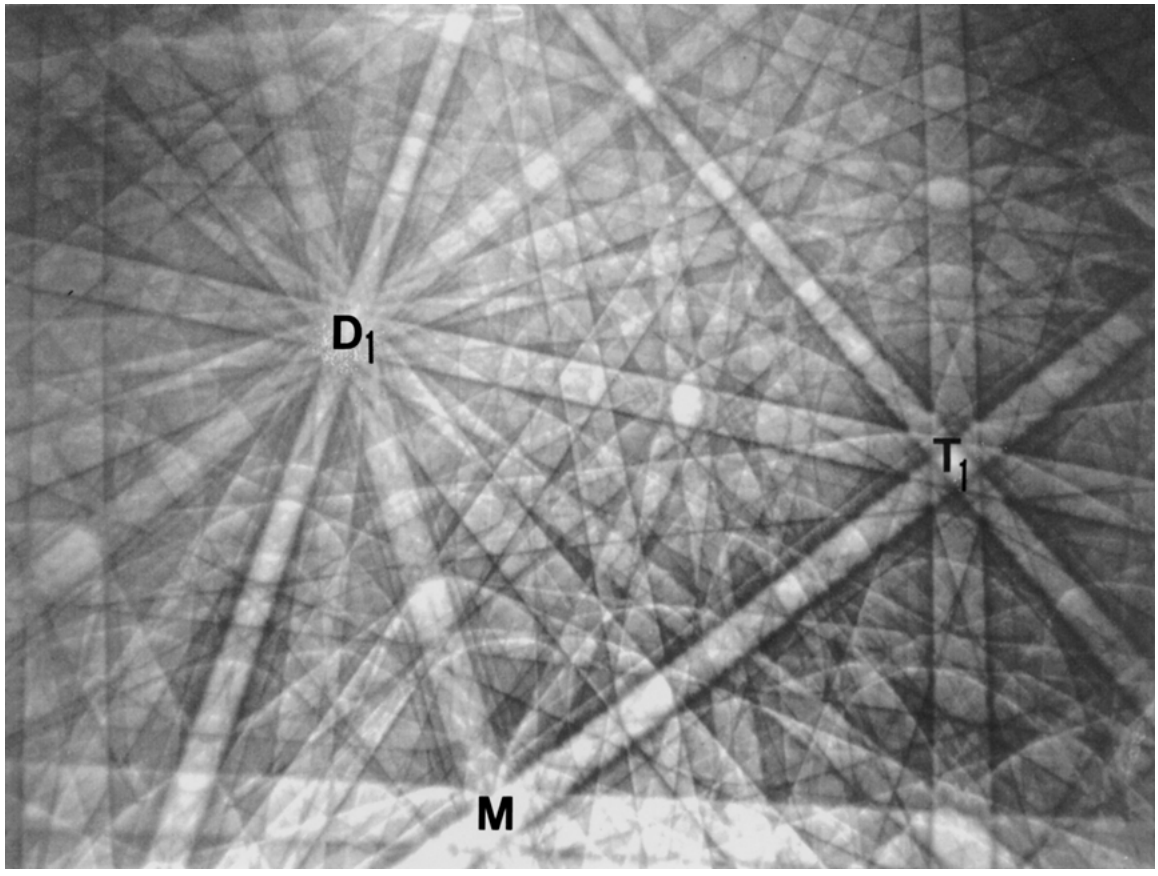

(a)

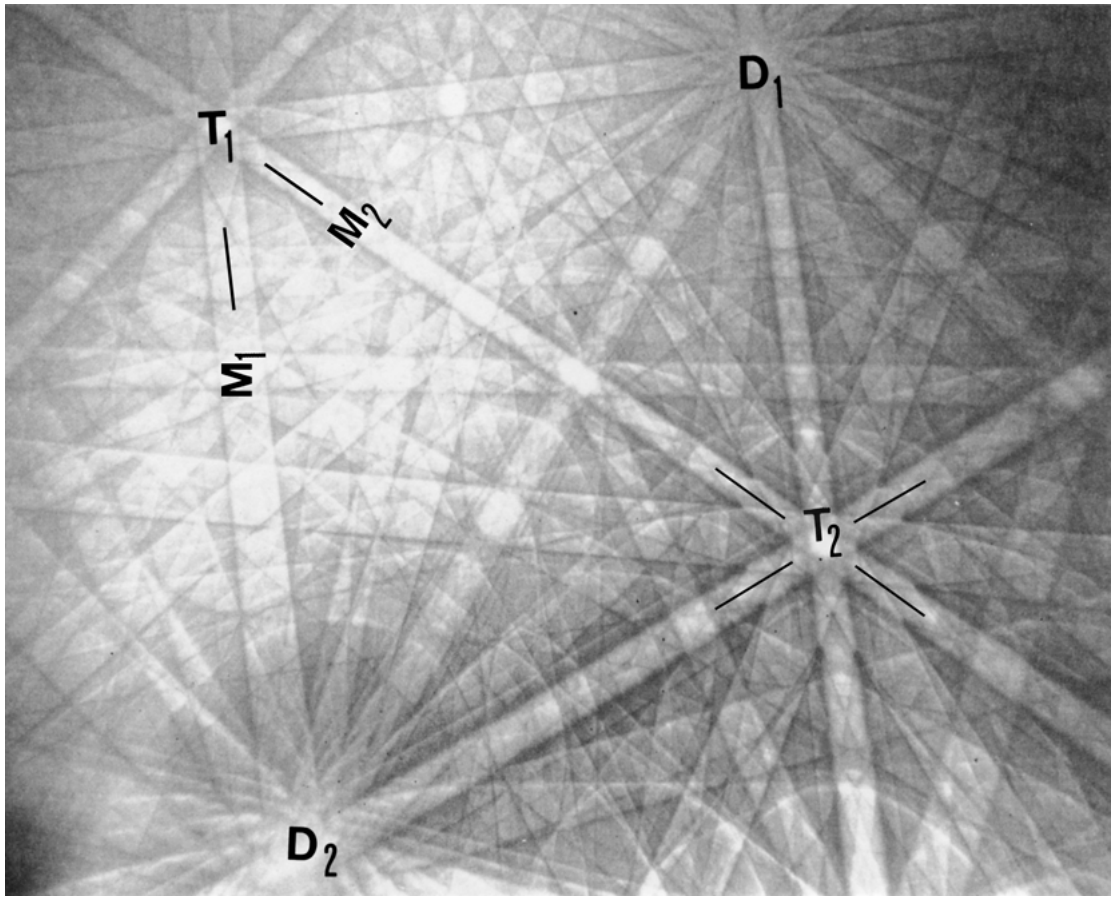

(b)

Figure 11 (a) BKDP from germanium showing the Laue groups 4*mm*, 2*mm* and *m*. T_1 and D_1 represent the [001] and [110] zone axes with Laue groups 4*mm* and 2*mm*, respectively. The reflections marked m_1, m_2 and uv were used to determine the Bravais lattice. The reflection uv is further illustrated in Fig. 13; (b) A wide-angle BKDP showing all the three essential zone axes, [001], [110], and [111], with Laue groups 4*mm*, 2*mm* and 3*m*. The combination is the isometric crystallographic point group $m\bar{3}$ or $m3m$. The triad axis with Laue group 3*m* and indices [111] is labelled T_2. The two diads are marked D_1 and D_2. The tetrad [001] is T_1.

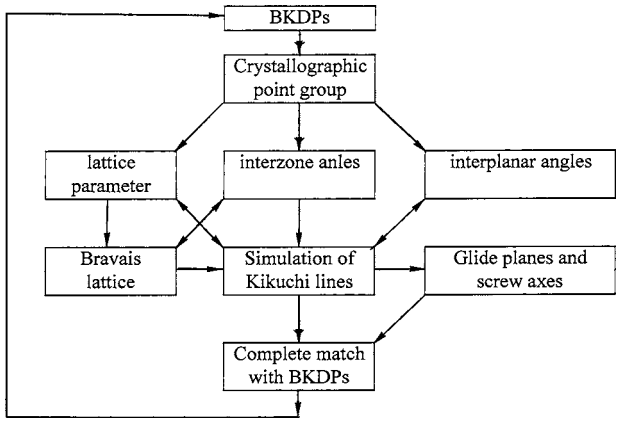

Figure 12 Diagram illustrating the procedures for space group determination using BKDPs.

lattice parameters before embarking on space group determination using BKDPs. This information, however, might not be available about small particles or mineral inclusions. The degree of difficulty with space group determination depends largely on the availability of initial crystallographic information, and the quality of the patterns recorded.

An outline of the step-by-step procedures required for space group determination is described in Fig. 12. If the point group is correctly determined, lattice parameters have to be calculated based on the measured interplanar spacings of the first-order reflections visible on the BKDP. Since the diffraction order, n, of a selected Kikuchi band could be unknown, the measured lattice parameters could, at least, be two orders of magnitude above or below its real value. In addition, the estimated accuracy of measured values is about 5%. This needs also be considered in the value of a lattice parameter measured on the patterns. In simulating the pattern, a Bravais lattice, glide planes and possible screw axes need also be assumed. Consequently, a large number of simulations based on a variety of variables needs be produced, before a satisfactory match with the BKDP can be obtained. Interzone angles are the most accurate of the parameters that can be measured on BKDPs. Zone axes lie on co-linear positions in the gnomonic, and that their centres can be identified with reasonable precision. In cubic crystals, interzone angles are fixed between zone axes, regardless of their space groups. The angular relationship in cubic crystals can be used as confirming the cubic symmetry. These angles can then be used to index the various zone axes. However, as the crystal symmetry is lowered, the complexity of space group determination increases significantly.

The procedures for space group determination using BKDPs have been fully described elsewhere [49]. To illustrate space group determination, BKDPs recorded from a crystal of germanium are briefly analyzed here.

8.4. The space group of germanium

The structure of germanium has been described in detail by various techniques [90]. The purpose of this discussion is to derive the space group $Fd\bar{3}m$ as an example of a methodology that can be used to derive space group using BKDPs.

In the BKDP, Fig. 11a, the zone axis labelled T_1 is common to four planes of reflection symmetry, marked with solid lines, represents the tetrad-axis ⟨100⟩ of germanium. The zone axis Laue group must therefore be $4mm$. In order to find all the other symmetry operations present in the patterns, we next study the diffraction patterns in Fig. 11b. It is easily seen that a mirror plane in T_1 intersects another prominent zone axis labelled T_2, which is also the point of intersection of two other planes of reflection symmetry. By measurement, the interzonal angle between T_1 and T_2 is 54°. The zone axis T_2 is therefore the triad axis ⟨111⟩ of the cubic cell, with Laue group $3m$. This implies that the zone axes labelled D_1 and D_2 must be diads ⟨110⟩ with the Laue groups $2mm$. Also, by measurement, the interaxes angles D_1T_1 and D_2T_1 were found to be 44.5°. Measurements show that the zone axis labelled M is situated 30° away from both D_1 and D_2. This means that M is a monad axis with Laue group m.

The combination of the Laue groups $4mm$, $3m$, $2mm$ and m derived from the patterns, signifies that the crystal is isometric cubic with the whole-pattern point group $m3m$.

In order to establish the Bravais lattice, the measured ratios of the d-spacings of the principal reflections are compared with the ratios of the planes parallel to (100), (110) and (111). The measured d-spacings corresponding to the Kikuchi bands m_1, m_2 and uv are 0.14 nm, 0.19 nm and 0.16 nm, respectively. If we inspect the (111) systematic row of reflections, shown enlarged in Fig. 13, and take their ratios, then they are not in systematic order. Therefore, it

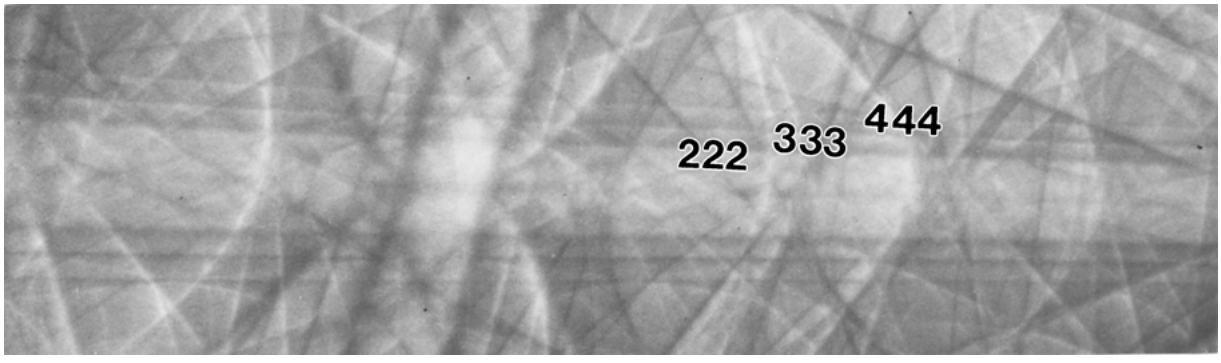

Figure 13 The (*hhh*) systematic row reflections in BKDP from germanium. The reflection (222) has a measured d-spacing 0.16 nm. The first-order (111) is invisible due to anomalous intensity within the band.

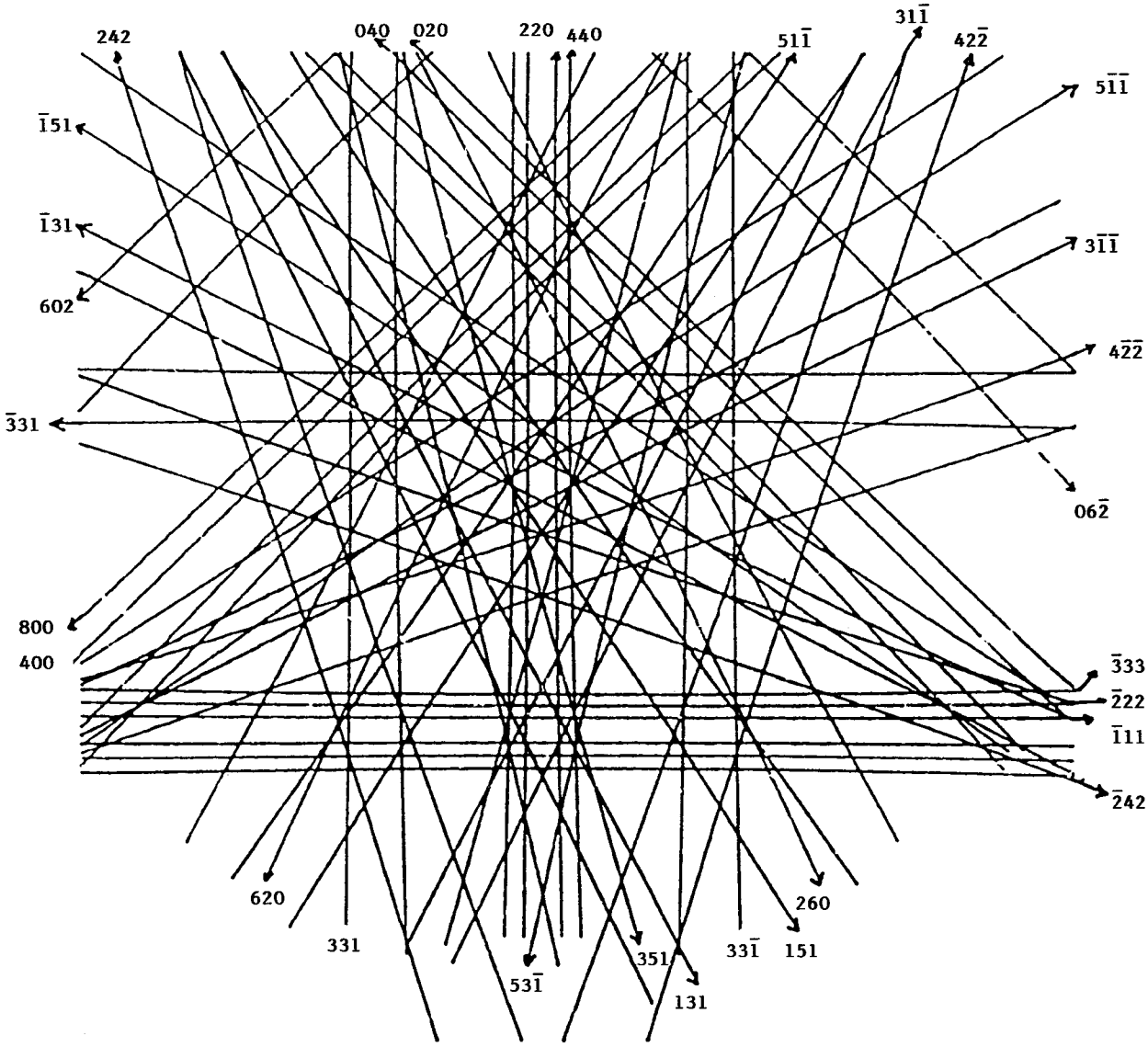

Figure 14 Computer simulation of the various Kikuchi lines observed in BKDP in Fig. 11. The lattice constant used for this simulation is $a = 0.56$ nm.

could be concluded that the (111) reflection is invisible because of anomalous effects described in Section 10. Hence, we deduce that the d-spacing of (111) is 0.32 nm. The ratios of the measured d-spacings are therefore $d(m_2) : d(m_1) : d(uv) = 1/1.36/2.29$. This closely corresponds to twice the standard ratios of $d(100) : d(110) : d(111) = 1 : 0.707 : 1.154$ in the F.C.C. lattice. These ratios enable us to deduce that the mirror planes m_1 and m_2 are (220) and (400), respectively. From the Kikuchi band (400) the lattice parameters 'a' can then be calculated as 0.56 nm.

So far, we have been able to deduce the isometric point group and the face centred Bravais lattice. To determine the complete space group, a detailed simulation of the BKDPs needs to be carried out using the lattice constant 0.56 nm. The computer-simulated map, in Fig. 14, is a good match with the corresponding diffraction patterns. To prevent overcrowding in the simulated pattern, only the essential reflections are plotted. To establish the space group, a comparison of the observed and absent reflections is carried out. It is seen in Table VI that the conditions for the absent

TABLE VI List of the observed and absent reflections in BKDPs recorded from germanium. The crystal is face-centred with a d-glide plane parallel to (001)

Class of reflections	Observed reflections	Absent reflections	Condition for reflections	Cause of reflections
hkl	331, 51$\bar{1}$ $\bar{1}$11, $\bar{2}$22 $\bar{3}$33, $\bar{3}$31 $\bar{1}$31, $\bar{1}$51 242, 131 351, 42$\bar{2}$ (*h*, *k*, 1 *permutable*)	21$\bar{1}$, 121 212 210	$h+k=2n$ $h+l=2n$ $k+l=2n$	Face-centred
hhl	331, 220 111, 222	110, 330 550	$h+l=2n$	Face-centred
0*kl*	06$\bar{2}$	03$\bar{1}$	$k+l=4n$ $k, l=2n$	d-glide parallel to (001)
*hk*0	620, 260 420	310, 130 210	$h+k=4n$ $h, k=2n$	d-glide parallel to (001)
*h*00	400	200, 300 100, 500	$h=4n$ $h+k=2n$	d-glide parallel to (001)

reflections satisfy a face-centred Bravais lattice with a d-glide parallel to {100}. The simulation carried out indicates that the reflections (200), (500), (310), (110), (330) and (121) are absent. The space group is therefore seen to be $Fd\bar{3}m$.

9. Special applications

9.1. Determination of crystallographic polarity

The crystals of diamond and germanium are centrosymmetric with space group $Fd\bar{3}m$. The space group $Fd\bar{3}m$ can change into the non-centrosymmetric $F\bar{4}3m$, which is common to many of the so-called Zincblende structures. The crystals that fall into this category include GaAs, InP, GaSb, and various minerals including zincblende (ZnS), and chalcopyrite ($CuFeS_2$).

The structural characteristic that distinguishes ZnS from diamond is that in ZnS, there is an alternate stacking sequence of Zn and S atoms parallel to the {111} crystal planes, Fig. 15a. This creates a polar [111] direction because the {111} planes differ in the organization of their atomic structures, compared with the same planes in diamond [91, 92]. The diffracted intensities in ordinary X-ray diffraction originating from this form of non-equivalent (111) planes, are identical, which do not permit a direct observation of lack of centre of symmetry. Consequently, Friedel's law, which states that $F^*F(h, k, l) = F^*F(\bar{h}, \bar{k}, \bar{\ell})$ is applicable to this form of X-ray diffraction [93]. Here F is the structure factor and F^* denotes the imaginary part of the structure factor. However, when the wavelength of the diffracted X-rays is close to the absorption edge of the constituent atoms, Friedel's law becomes no longer valid [94].

Using certain electron diffraction techniques, non-equivalent intensities originating from the sensitivity of dynamical scattering to phases of the structure factors, can be observed. These techniques include convergent electron beam and electron channelling patterns [95, 96]. The dynamical theory of electron channelling patterns has been revised, which includes inter-Blochwaves intensity expressions, elucidating non-equivalent intensities arising from symmetrically unrelated atom planes in GaSb [97]. The non-equivalent intensities calculated for $51\bar{1}$ and $5\bar{1}\bar{1}$ reflections in GaSb are shown in Fig. 15b. BKDPs have also proved effective in determining the lack of centre of symmetry in a variety of materials [51, 52]. Using BKDPs, non-equivalent intensities have been observed in GaAs, GaSb, ZnS and the mineral tetraheadrite [51, 52]. To illustrate the form of non-equivalent intensities, BKDPs recorded from germanium and ZnS are shown in Figs 16a and b, respectively. Inspection shows that the reflections $51\bar{1}$ and $5\bar{1}\bar{1}$ from germanium have the same intensities, whereas in ZnS, the same reflections have different intensities. This is seen to confirm the lack of centre of symmetry in ZnS, i.e. the plane (200) is not a mirror reflection in all the zincblende structures.

9.2. Use of BKDPs in fine symmetry determination

It has been established that Kikuchi lines intersecting within systematic rows of reflections are very sensitive to lattice displacements, and small differences in interplanar spacings [40, 52]. These useful characteristics of Kikuchi lines intersecting within systematic rows, can be best illustrated using the diffraction patterns obtained from a crystal of chalcopyrite $CuFeS_2$ [52].

Chalcopyrite has point group $4\bar{2}m$ and space group $I\bar{4}2d$, which have been studied extensively [98]. The perspective structure of chalcopyrite is shown in Fig. 17, which is a double ZnS-type structure. The special problem associated with determination of the point group, $4\bar{2}m$, using BKDPs is to find reflections that have non-equivalent intensities, and therefore prove the breakdown of Friedel's law, analogous with ZnS. This has been studied in some detail and the results can be found in [51]. In addition, it is necessary to observe other asymmetrical details on BKDPs in order to determine the whole-crystal point group $4\bar{2}m$. Although chalcopyrite has ZnS structure, it is not cubic and has a tetragonal symmetry. According to $4\bar{2}m$, unlike the cubic ZnS, the zone axes [010] and [100] lie on rotation diads. Consequently, the reflections $0\bar{2}4$ and $02\bar{4}$, $20\bar{4}$ and $\bar{2}04$, which are the systematic row reflections parallel to [100] and [010] respectively, do not lie on mirror planes. The important aspect is that the c/a ratio of chalcopyrite is 1.969, indicating that any asymmetrical features

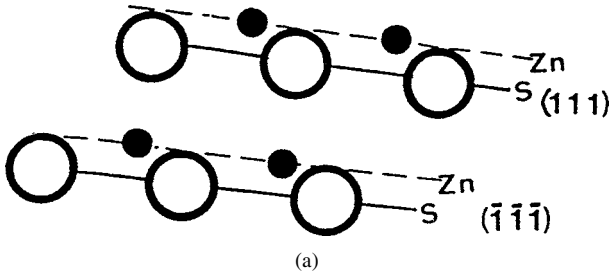

(a)

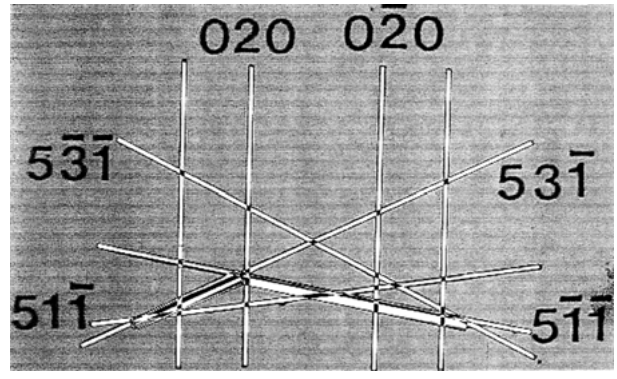

(b)

Figure 15 (a) The stacking sequence of the Zn and S atoms along the (111) and ($\bar{1}\bar{1}\bar{1}$) crystal planes in Zincblende or sphalerite (ZnS). These planes are not equivalent, which result in the loss of centre of symmetry in ZnS, (b) The intensities of the ($51\bar{1}$) and ($5\bar{1}\bar{1}$) reflections are calculated using the dynamical theory of electron diffraction, showing non-equivalent intensities between them. For clarity, the intensities are exaggerated.

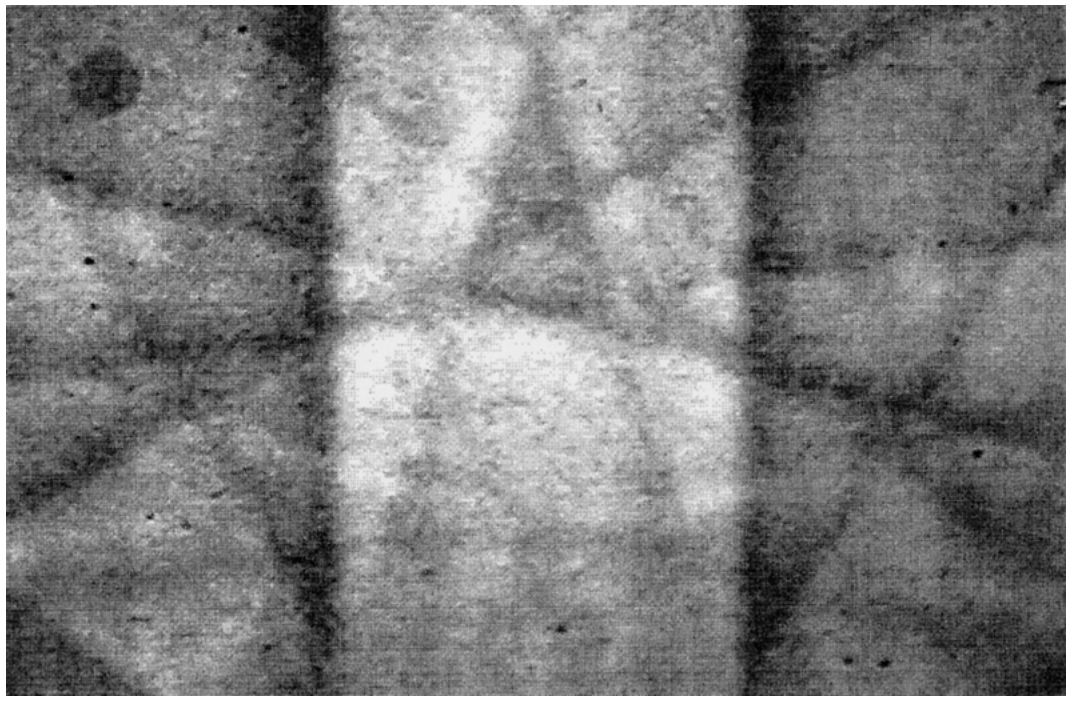

(a)

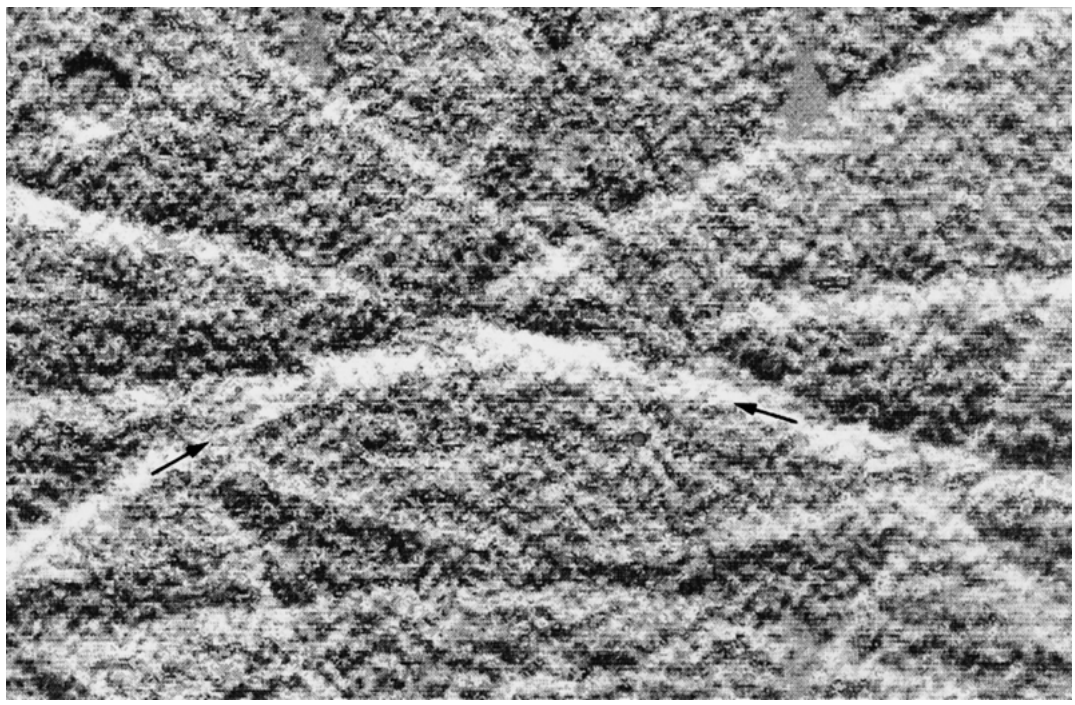

(b)

Figure 16 (a) BKDP from germanium showing the $(51\bar{1})$ and $(5\bar{1}\bar{1})$ reflections which have equal intensities. The symmetrical intensity along the arch, indicated with arrows, is easily visible; (b) BKDP from ZnS showing the $(51\bar{1})$ and $(5\bar{1}\bar{1})$ reflections, which have unequal intensities. The asymmetrical regions are shown with arrows. Both the patterns are processed to enhance the visibility of the intensities.

on BKDPs recorded from chalcopyrite must be subtle, and difficult to distinguish from BKDPs recorded from ZnS. The value of c/a is 1.969, when halved, is $1.969/2 = 0.9849$, being close to unity. The symmetry features of BKDPs in the cubic zincblende and that of the tetragonal chalcopyrite would be very similar, since the tetragonal distortion in chalcopyrite is very small. To observe this asymmetry, certain Kikuchi lines have been found in BKDPs from chalcopyrite, whose interplanar distances differ by a small amount, as shown in Table VII. The ratio of the reflections $3,3,\bar{1}\bar{4}$ and $\bar{3}7\bar{6}$ which intersect on $0\bar{2}4$ and $02\bar{4}$ systematic row is 0.991. Although small, this difference would cause a shift of the intersection point of the Kikuchi lines $3,3,\bar{1}\bar{4}$ and $\bar{3}7\bar{6}$ within $0\bar{2}4$ and $02\bar{4}$ systematic row. Fig. 18a shows a shift at the intersection point of the reflections $3,3,\bar{1}\bar{4}$ and $\bar{3}7\bar{6}$. This shift is relative to $0\bar{2}4$ and $\bar{0}24$, indicating that $0\bar{2}4$ and $\bar{0}24$ do not lie on mirror lines, see also the inset of Fig. 18a. To compare this observation with reflections that lie on mirror planes, the systematic row reflections 020 and $0\bar{2}0$ from chalcopyrite are illustrated in Fig. 18b and c. It can be seen that all the reflections intersect precisely within the systematic row 020 and $0\bar{2}0$. The point group of chalcopyrite is therefore $4\bar{2}m$.

TABLE VII Calculated and measured interplanar angles for certain reflections in chalcopyrite. The interplanar ratios of these reflections are also included

Interplanar angles (°)			
Reflections	Calculated	Measured	Interplanar ratio
$3,3,\overline{14} - \bar{3}76$	60.3	59	0.991
$\bar{3},\bar{1},10 - 3\bar{5}2$	88.1	89	0.990
$\bar{5},\bar{1},14 - 5\bar{7}2$	98.2	100	0.991
$\bar{5},1,10 - 5\bar{5}\bar{2}$	133.2	133	0.993
$\bar{5}52 - 5,\bar{1},\bar{10}$	133.2	132	1.007
$\bar{3}16 - 3\bar{3}\bar{2}$	142.0	143	0.994

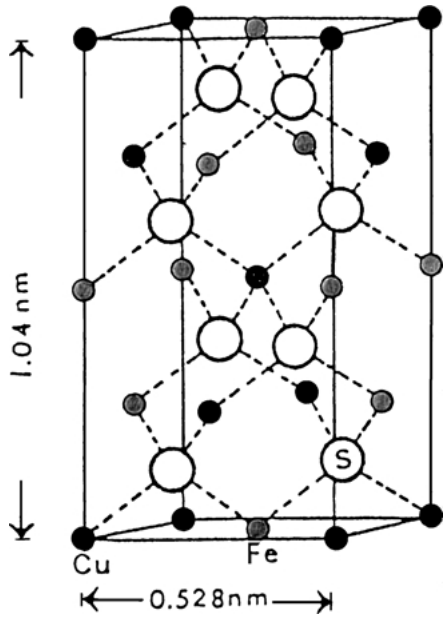

Figure 17 Perspective crystal structure of chalcopyrite, showing a double Zincblende (ZnS) unit cell. The ordered arrangement of the Cu, Fe, and S ions is tetrahedrally co-ordinated in a manner identical to sphalerite (ZnS).

For computer simulated patterns of these results, the reader is referred to Baba-Kishi [40].

9.3. Orientation microscopy

A comprehensive analysis and discussion of orientation microscopy is beyond the scope of this article. Here, only a brief description of the technique together with a list of references is provided.

Determination of the macro-texture of polycrystalline materials is a well-known problem and is often performed by X-ray diffraction methods [99, 100]. The information gained about texture is useful to quality control and assessment of material properties, including certain deformation characteristics. The distribution of grain orientations in a random or non-random manner has direct relevance to material performance.

An important feature of BKDPs is in its capability to carry out a large number of crystal orientation measurements by automated methods. This is performed by randomly analyzing a percentage of data points across a selected grid on the specimen. Automated analysis requires specific software modules for data retrieval and analysis and for beam control. Computer-controlled SEM stage controller, and a beam control software are also required.

The manually operated BKDPs uses camera-controller, image processor, frame grabber together with an appropriate software to carry out orientation measurements. In the automated approach, the stage controller and the beam control hardware work in conjunction with software to carry out numerous measurements on a selected grid of a polycrystalline specimen. An important application of orientation microscopy is the study of relationship between orientation and nearest-neighbor grain with respect to micro-texture, mesotexture, grain growth and properties.

Orientation microscopy or micro-texture analysis in the SEM has become a widely used application of BKDPs, capable of providing overall or local texture information in polycrystalline materials [100–102]. The experimental arrangement for orientation microscopy is shown in Fig. 6b. The arrangement is essentially the same as that used to record BKDPs for phase identification. The major difference between the two methods is that the recorded pattern for texture microscopy is processed with the aid of software in order to extract orientation information. There are now various commercial software and hardware packages, allowing semi-automatic or automatic orientation analysis.

The basic concept of orientation microscopy is to superimpose a computer generated cursor onto the diffraction screen. The cursor is used to identify various different zone axes on a BKDP. The positions of the zone axes are then measured, indexed automatically and converted into orientation information. In order to determine the orientation of a particular pattern, the zone axes are defined in terms of vectors drawn from the electron source point within the sample. The specimen to screen distance, the pattern centre and the crystallographic parameters of the specimen under investigation must be known in advance of any orientation microscopy. The results of all the measured orientations are displayed in a pole-figure projection, which essentially represent all the orientations within the stereographic projection. An example is shown in Fig. 19, which a [100] microtexture stereographic pole-figure consisting of 500 plane orientations obtained using BKDPs.

There is a more recent addition to orientation microscopy, termed as Orientation Imaging Microscopy [103–105]. The technique involves forming contrast from local variations in grain orientations, allowing local cracks, and grain boundaries to be imaged. It also allows spatial distribution of grain texture over the entire sampling area to be determined. Since the technique requires a large number of measurements, a fully automated approach is necessary. The automated control includes the specimen stage, pattern recording procedures, and the image-analysis program [104]. Additional references are provided on the following topics. Orientations microscopy and automated detection [106–112], On-line analysis and applications of BKDPs [113–116], study of fatigue and deformation [117–122], misorientation [123], strain [124], grain boundaries [125–128] and orientation studies [129–135].

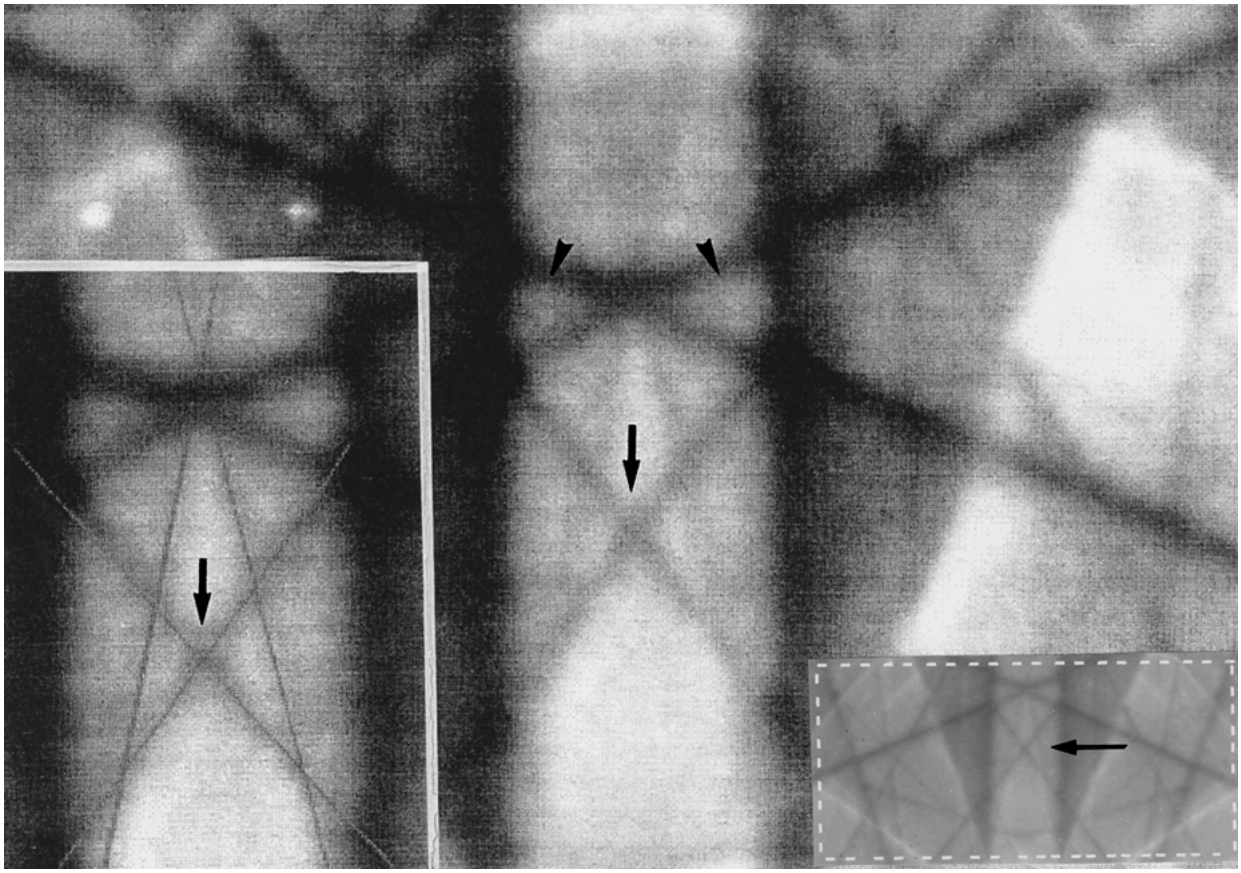

(a)

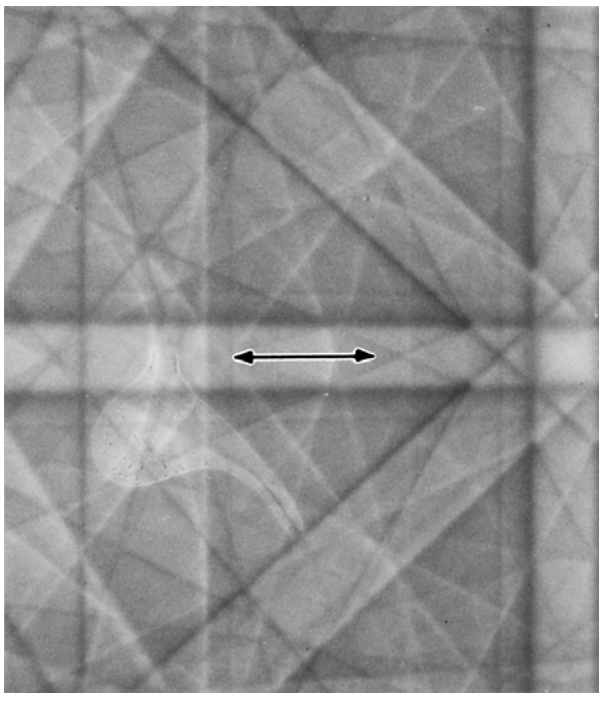

(b)

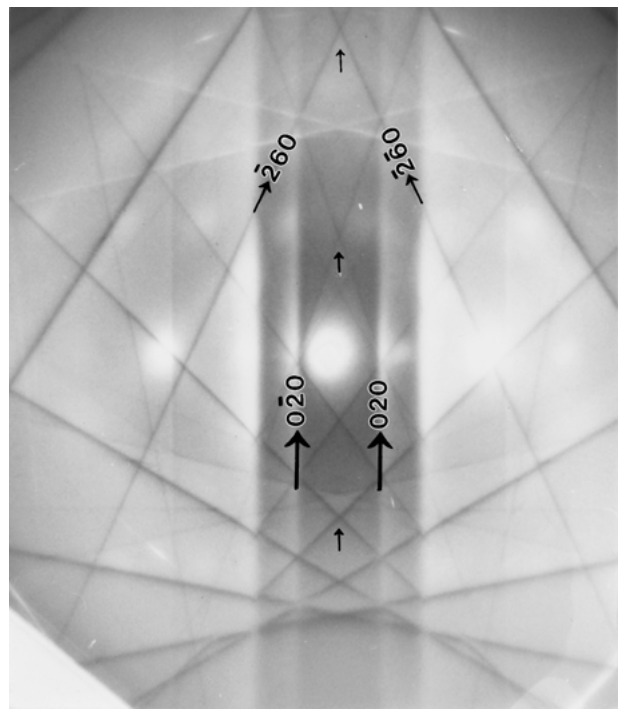

(c)

Figure 18 (a) Kikuchi lines from chalcopyrite intersecting within the $0\bar{2}4$ and $02\bar{4}$, showing a shift towards the right, arrowed. This shift at the intersection point originates from the tetragonal structure of chalcopyrite. The reflections $\bar{2}04$ and $02\bar{4}$ do not lie on a mirror plane. Small arrows point to two triangles of different sizes. The large arrow points to the centre of the band. Inset: Lines drawn over the Kikuchi lines to indicate the asymmetry of the intersections with respect to the large black arrow; (b) Kikuchi lines from chalcopyrite intersecting within the 020 and $0\bar{2}0$ systematic row. There is no shift at the intersection points of the Kikuchi lines intersecting within the systematic row. The reflections 020 and $0\bar{2}0$ lie on a mirror plane; (c) Diffraction pattern recorded in the TEM showing the 020 and $0\bar{2}0$ systematic row as a mirror plane, consistent with Fig. 18b.

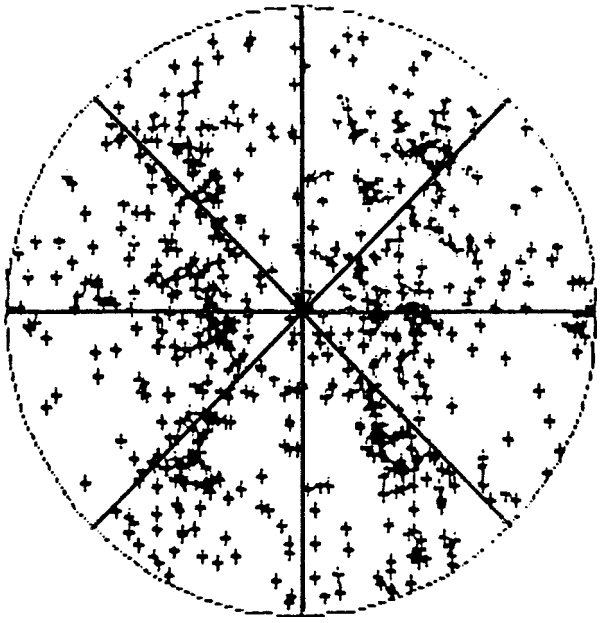

Figure 19 Stereographic pole-figure illustrating grain orientations in an annealed [100] copper specimen.

In a recent study reported by Humphreys *et al.* [136], the precision of the technique has been increased by the use of data averaging. The use of certain parameters and filters allow a reduction in orientation by about 10 times. In another recent review article, Humphreys [137] describes the use of Field Emission SEM for quantitative analysis of grains and sub-grains down to about 0.2 μm. It is shown that automated BKDPs can provide texture information that can be correlated with grain or sub-grain size, shape and positions. Using automated BKDPs (EBDS) spatial distribution of stored energy in a sample, the quantity of recrystallization and boundary misorientations can be routinely measured.

9.4. Strain measurements using BKDPs

An area of application where BKDPs are of some use, is measurement of plastic strains. Quested [138] used BKDPs for an evaluation of plastic strains, which involved measurement of decreasing sharpness in Kikuchi band edges, as a function of increasing strain. Kikuchi bands become diffuse or less sharp as the crystal undergoes deformation because of bending or dislocations within the crystal structure [139].

The accuracy of plastic strain measurements is about 5%. The main problem with the measurement of diffuse Kikuchi line edges is the difficulty in locating a band edge with sufficient precision before and after deformation. Low-order Kikuchi band edges are generally diffuse because of electron channelling effects and strong inelastic scattering. High-order Kikuchi band edges generally yield better accuracy and precision. High-order Kikuchi lines of sufficiently high intensity need to be selected for this purpose, but might not be readily visible because of background intensity gradient.

Prior to the use of BKDPs for elastic strains measurements, selected area channelling patterns (SACP) were used for this purpose [140]. High-Order Laue zone (HOLZ) rings within SADPs are particularly sensitive to changes in the lattice parameter and to elastic strains: they slightly shift from their original positions upon the application of strain. The use of HOLZ rings can provide an accurate measure of elastic strains. An advantage of SADPs lies in producing distortion-free HOLZ rings. However, SADPs require a large, flat and relatively clean surface in order to produce a satisfactory contrast. A notable feature of a BKDP or SADP originating from a strained material, is deterioration in the quality of the pattern, accompanied by changes in the widths of certain Kikuchi bands.

Wilkinson [141–143] also used BKDPs for evaluation of elastic strain upon deformation. The observations were based on decrease in the quality and sharpness of Kikuchi bands arising from deformation. Troost *et al.* [53], carried out elastic strains measurements capable of μm resolution using both BKDPs and X-rays. They correlated the results of their high-resolution X-ray diffraction studies with BKDPs and found a good agreement between them. They noted a displacement in the position of the $(02\bar{2})$ band, recorded from a strained sample of $Si_{(1-x)}Ge_x$ grown on (100) silicon. For a value of $x = 0.34$, the measured perpendicular elastic strain using BKDPs was 2.5%, achieving an accuracy of 0.1%.

An alternative method for determination of elastic strains and tetragonal dislocation of epitaxial layers in $Si_{(1-x)}G_x$ on silicon, with $x = 0.2$ and 0.05, has been described by Wilkinson [54]. The method involves reducing the capture angle of BKDPs by increasing the specimen-to-film distance to about 140 mm, from a standard distance of ~30 mm. A reduction in the capture angle by ~14° has been achieved in this way. An example of a BKDP recorded at an extended specimen-to-film distance is shown in Fig. 20. Combined with image analysis procedures, interzone angles and shifts in the positions of Kikuchi lines have been measured. The work of Wilkinson describes a technique with high spatial resolution, capable of sensitivity to elastic strains of the order 0.02%. In measuring the tetragonal lattice distortion, an accuracy of 0.01° has been achieved, which is an improvement of two orders of magnitude compared with wide-angle BKDPs.

10. Anomalies in BKDPs

Backscatter Kikuchi diffraction patterns are the result of multiple elastic and inelastic scattering processes. Since the patterns originate from deep in the specimen, the influence of dynamical scattering becomes significant. The most important anomaly arises from dynamically generated patterns that are interpreted using the kinematical scattering rules. Low-order Kikuchi bands or systematic rows of reflections are mainly influenced by dynamically scattered intensities; intensity irregularity along the band edges, and high contrast within the bands are clearly the manifestations of dynamical scattering. Using Kinematical assumptions, high-order Kikuchi bands can be used for crystallographic analysis. It is considered that energy losses associated with high-order lines during scattering are minimal. Electron channelling effects are also negligible in high-order

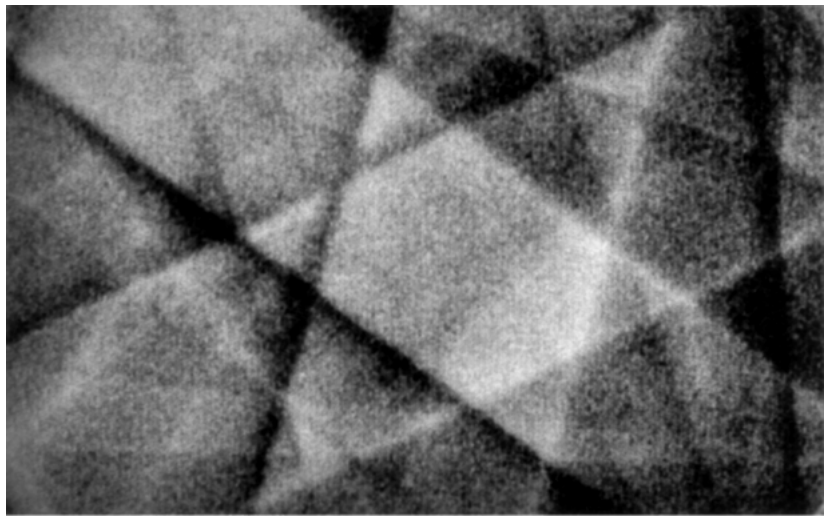

Figure 20 BKDP recorded on film from a crystal of silicon, using a long specimen-to-film distance with a capture angles ∼14°. The capture angle of the BKDP is significantly reduced, allowing precise measurements. Courtesy of A. J. Wilkinson.

Kikuchi lines. Critical-voltage effects and splitting of Kikuchi lines due to dynamical scattering are not easily observable in BKDPs. However, when BKDPs are used for crystallographic purposes, care is needed to avoid anomalies arising from dynamical structure factor considerations. The two most commonly encountered anomalies are described below.

10.1. Anomalous invisibility

An important anomalous effect commonly encountered in BKDPs is that certain reflections permitted by the structure factors become invisible. There are two reasons for this invisibility:

1. electron channelling and
2. structure factor considerations. To illustrate the problem, BKDPs recorded from $TaTe_4$ are discussed.

$TaTe_4$ has the possible space groups P4/*mmc*, P4/*mcc* and P4*cc*, being therefore primitive, allowing all orders of reflections to be present with the exception of *hhl* with *l*#2*n* reflections. This originates from the c-glide plane. The reflections (110), (220), and (330) along the systematic row (*hh*0), and the reflections (100), (200), (300) and (400) along the systematic row (*h*00) must therefore be visible. However, BKDPs recorded from $TaTe_4$ only reveal (300) and (400) along (*h*00), Fig. 21a. The remaining reflections are anomalously invisible. Convergent beam electron diffraction patterns obtained in the TEM from $TaTe_4$ also show similar anomalous effects, Fig. 21b. Studies carried out indicate that the cause of the invisibly is the combination of both the electron channelling and structure factor considerations, described below.

Initially, dispersion surfaces were calculated for the systematic row *h*00, for normal incidence along [001] at 120 kV [144]. The dispersion surfaces indicate that the Bloch waves for the reciprocal lattice points 1/2 g, g, 3/2 g and 2 g, corresponding to the reflections 100, 200, 300 and 400 are strongly excited, i.e. these reflections must be present in the diffraction patterns, Fig. 22. The first two branches of the dispersion surface are flat, indicating that the Bloch wave excitations do not vary significantly with changes in the orientations and that the Bloch waves are localized on the atomic strings [144]. To illustrate these, spatial variations of the Bloch wave amplitudes across the (*h*00) projected planar unit cell in

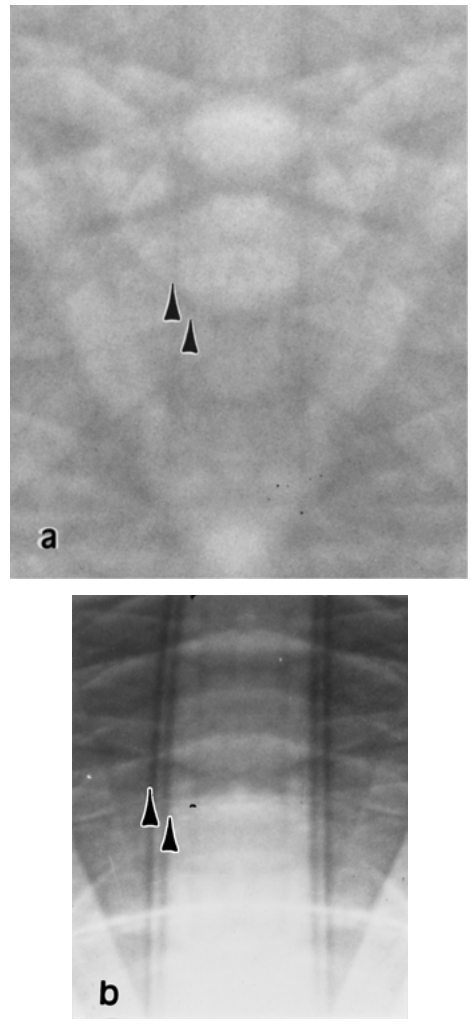

Figure 21 (a) BKDP and b) CBED showing the (*h*00) systematic row of reflections in $TaTe_4$. The reflections (100), (200), (300) and (400) are allowed, but only the (300) and (400) reflections, indicated with arrows, can be observed with clarity in the patterns.

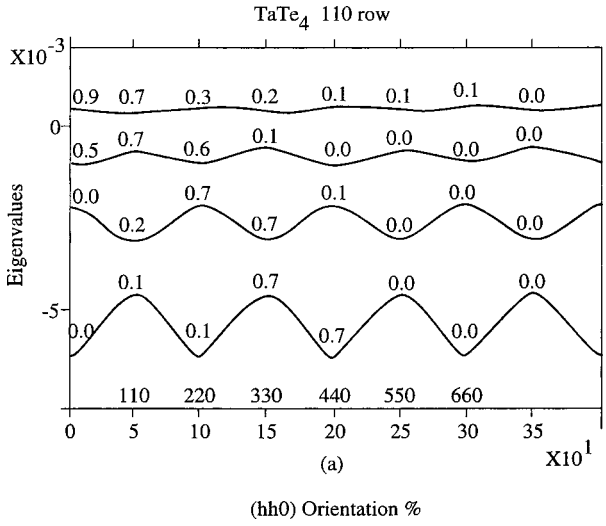

Figure 22 Dispersion surfaces calculated for the (h00) systematic row of reflections in $TaTe_4$. The reflections (100), (200), (300) and (400) are strongly excited, and should be present in the diffraction patterns. The numbers above the curves indicate the degree of excitation of the Bloch waves associated with a particular reflection.

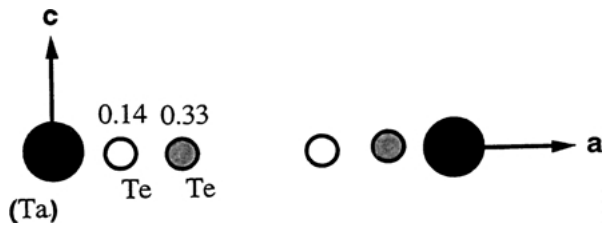

Figure 23 Schematic showing the one-dimensional projected unit cell in $TaTe_4$ for the (h00) systematic row, along the a-direction. The numbers indicate the heights of the atoms.

real-space for various angles of incidence were plotted. The plots correspond to the Fourier Transforms of the Eigenvectors across a one-dimensional projected cell. The orientations plotted, describe the angular range in a convergent beam disc with a 1° convergence. The plots indicate that the Bloch wave amplitudes vary little over this orientation range, and therefore the amplitudes are highly peaked, being localized at the Ta and Te atomic sites, close to the Bragg positions. The one-dimensional structure of $TaTe_4$ is shown in Fig. 23. The plots of the Bloch wave amplitudes are shown in Figs 24a–f.

Dynamical backscattered intensity profiles calculated across the (h00) row, illustrate little intensity variations between 100, 200 and 300, as shown in Fig. 25. The diffracted intensities of these reflections remain constant across the entire systematic row (h00).

The causes of the invisibility of these reflections in BKDPs can therefore be described as a combination of Bloch waves localized on the atomic strings, and the constancy in the diffracted intensities. Consequently, these reflections merge into each other, creating a single, broad Kikuchi band, causing the various individual reflections to become indistinguishable. This form of anomalous effect is quite common in Kikuchi patterns.

10.2. Overcrowded BKDPs

There are certain crystals that possess a combination of large lattice parameters, superstructures and primitive

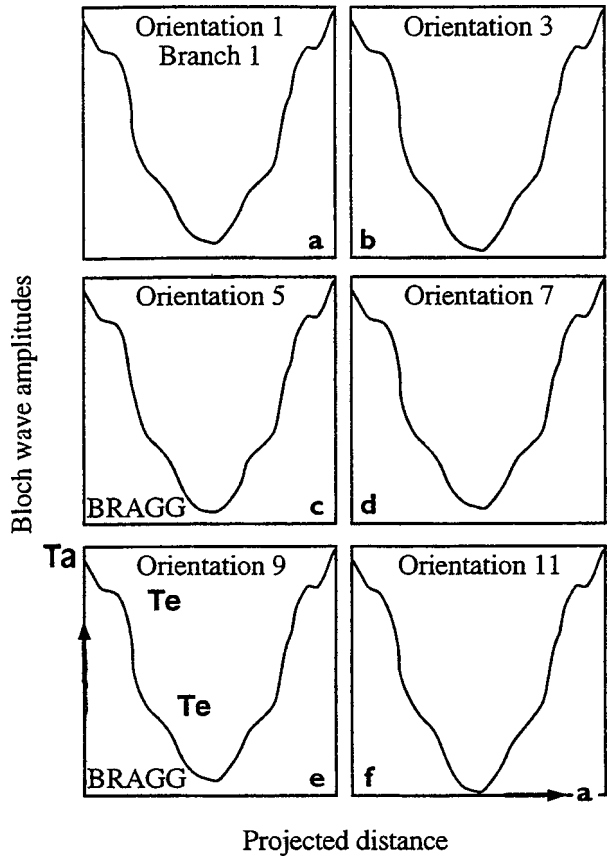

Figure 24 Plots showing the magnitudes of the Bloch wave amplitudes across the one-dimensional unit cell (Fig. 23), for branch one of the (h00) row. The plots are the Fourier Transforms of the Eigen vectors across the unit cell. Each plot corresponds to a slightly different orientation. The positions of Ta and Te are marked.

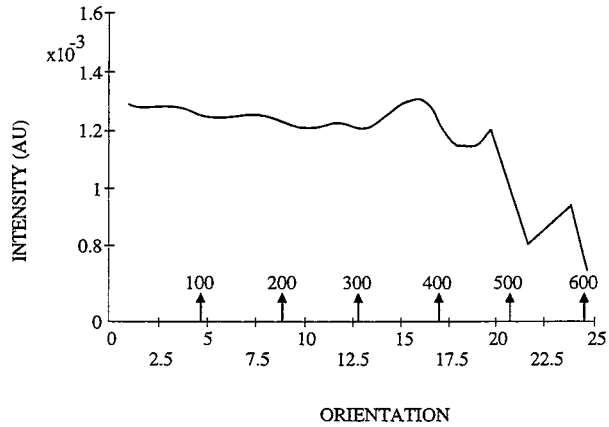

Figure 25 Theoretical backscattered intensity profile calculated across the (h00) systematic row of reflections at 30 kV for $TaTe_4$. There is little variation in intensity between (100), (200) and (300).

unit cells. In such crystals, the number of reciprocal lattice points contained within the sphere of reflection is large, leading to numerous reflections; mostly high-order reflections. An example is the crystal of $Er_2Ge_2O_7$, which has a primitive tetragonal structure, space group $P4_1cc$ with lattice parameters $a = 6.778$ Å, $b = 6.778$ Å and $c = 12.34$ Å. A BKDP recorded from $Er_2Ge_2O_7$ is shown in Fig. 26. The pattern contains numerous reflections and a large number of high-order Laue zone (HOLZ) rings. The rings indicate the presence of a large number of high-order reflections, which

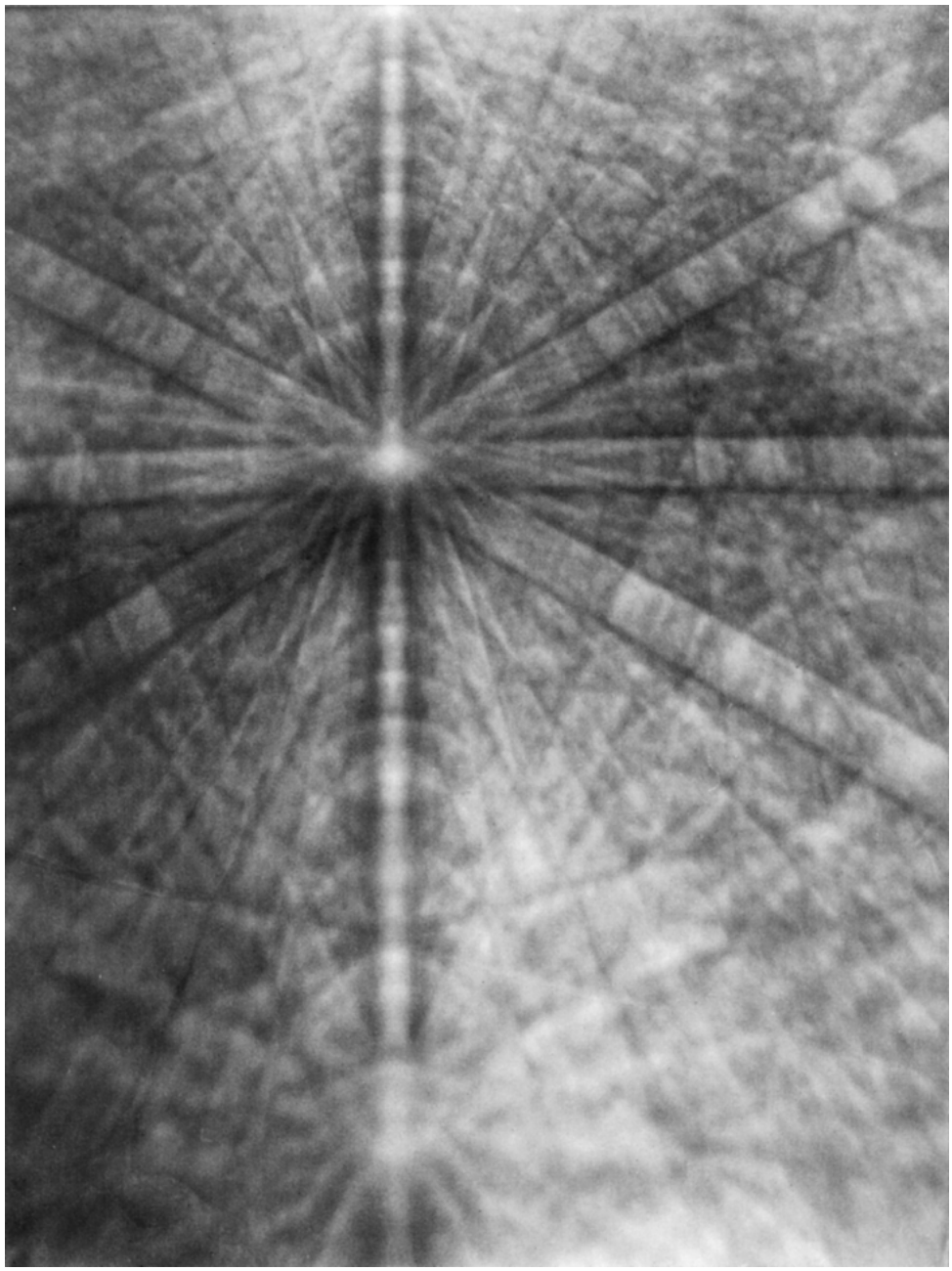

Figure 26 BKDP recorded from a crystal of $Er_2Ge_2O_7$, showing excessive overcrowding. There are many HOLZ rings due to the presence of a large number of high-order reflections. Point group or space group determination using such a pattern would be highly ambiguous.

could be used to obtain important crystallographic information about a crystal. An excellent example of the use of HOLZ rings to measure reciprocal lattice layer spacing in BKDPs is described by Michael *et al*. [145].

The most important feature of the pattern in Fig. 26 is the presence of numerous weak reflections, which tend to merge into other Kikuchi bands, leading to a uniform background contrast. Since the point group of $Er_2Ge_2O_7$ is known, it is possible to arrive at some conclusion about the presence of the four-fold rotation axis. In practice however, it would be impossible to reach a definite conclusion about the projected crystal symmetry. The pattern is simply too crowded to allow an unambiguous crystal symmetry determination.

Substantial developments in automated phase identification and crystal structure determination using a combination of BKDPs and EDX have also been reported by Michael [146]. Such automated phase identification enables a routine identification and measurements of the positions and widths of the Kikuchi bands on the diffraction patterns, allowing the unit cell volume to be calculated. These coupled with the chemical information extracted using EDX microanalysis, allow a search in database of crystal structures. Ultimately, however, the ensuing crystal structure needs to be carefully reassessed to avoid anomalous effects that are inherent to BKDPs.

10.3. Structure factors

Structure factor considerations alone might lead to ambiguity in BKDPs. To illustrate the situation, a BKDP showing the $h00$ systematic row from GaAs is shown in Fig. 27a. The corresponding dynamically calculated intensity profile across the $h00$ reflections is also shown in Fig. 27b.

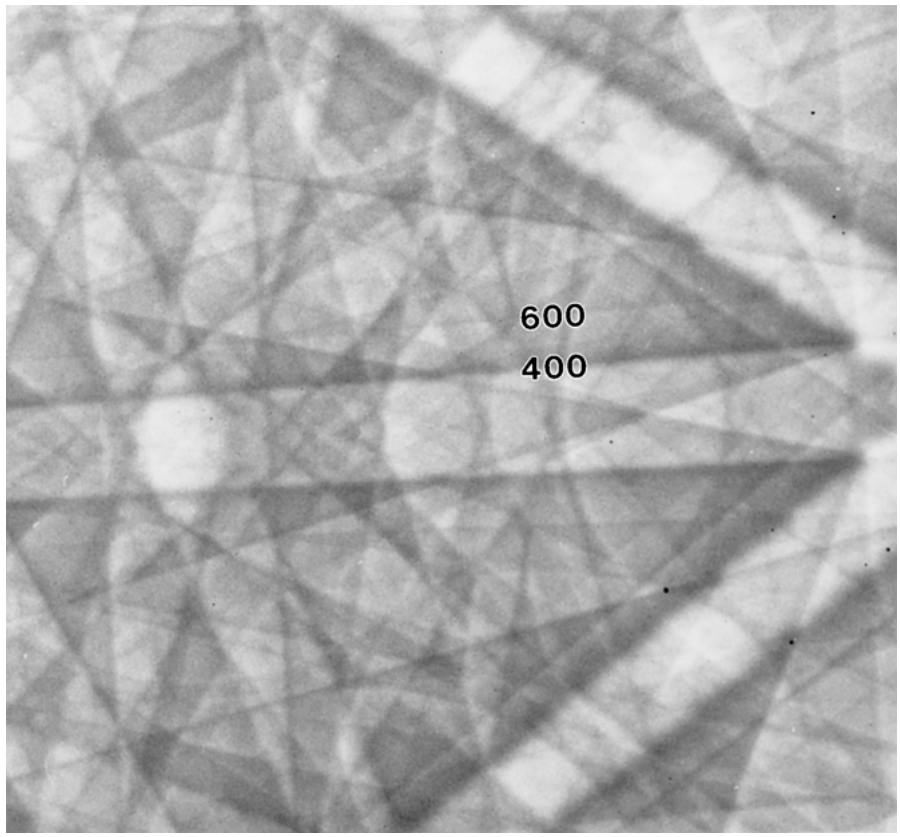

(a)

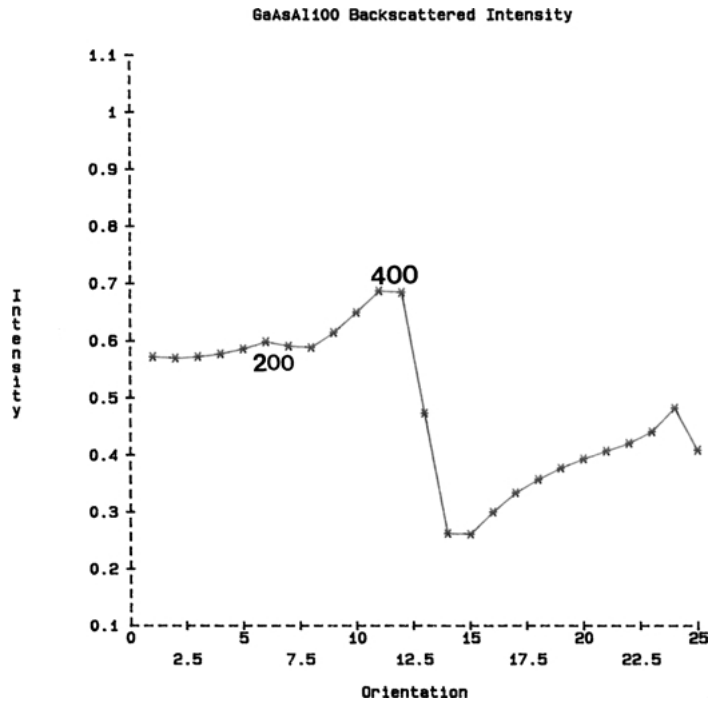

(b)

Figure 27 (a) BKDP from (h00) systematic row in GaAs. The Kikuchi band visible in the pattern is (400). The band (200) is also permitted, but has a weak intensity, becoming invisible inside (400). (b) Theoretical backscattered intensity profile calculated across the (h00) systematic row for GaAs, showing a strong peak associated with (400). The small peak (arrowed) corresponds to (200), which has very weak intensity.

An examination of the systematic band (h00) in the BKDP from GaAs, shows only a single first-order reflection present. This is the (400) reflection permitted by the space group $F\bar{4}3m$. In addition, the reflection (200) is also permitted in GaAs, but is not readily visible in the pattern. The calculated dynamical intensity profile indicates that the (200) reflection is indeed present, but has significantly weaker intensity at the Bragg position compared with (400). Evidently, the intensity of (200) is very weak compared with (400). For this reason, the weak (200) reflection, which has a larger d-spacing and must appear within the strong (400), becomes invisible in the pattern. This form of invisibility is an anomalous absence caused by the structure factor

considerations. This situation can apply to many crystals, including chalcopyrite and tetrahedrite as discussed in Baba-Kishi [51].

11. Conclusions

It is demonstrated that BKDPs have a variety of applications, including point group, and space group determination, microtexture and orientation imaging microscopy, and strain analysis. An important advantage of BKDPs over other diffraction techniques is seen to lie in its wide-angular diffraction coverage, enabling large-area diffraction patterns from sub-micron regions to be recorded. Using BKDPs, detailed crystallographic analysis in real-space can be carried out, allowing three-dimensional point group to be determined by combining individual Laue groups. Space group determination by BKDPs is possible, requiring a variety of measurements on the patterns, crystallographic indexing, and extensive computer simulation of Kikuchi lines.

It was shown that the dynamical theory of electron diffraction could be used as an aid in the interpretation of certain crystallographic and anomalous characteristics in BKDPs. A special application of BKDPs includes the use of the sensitivity of dynamical scattering to phases of the structure factors to determine crystallographic polarity. Another special application of the technique is the use of Kikuchi lines intersections within systematic rows of reflections to determine small crystal distortions. Anomalous scattering associated with electron channelling within certain atomic strings, problems associated with over-crowded patterns and certain structure factor considerations are discussed. It is seen that dynamical scattering, combined with structure factors could cause Kikuchi lines to merge into each other, leading to ambiguity in symmetry determination.

In conclusion, it is evident that BKDPs is a powerful and versatile technique in the scanning electron microscope, and can be used in a variety of ways to deduce crystallographic, strain, and orientation information about a variety of materials.

References

1. D. C. JOY, "Electron Microscopy-Principles and Applications," edited by S. Amelinckx, D. van Dyck, J. van Landuyt and G. van Tendeloo (VCH, A Wiley Company, 1997) p. 305.
2. L. REIMER, "Scanning Electron Microscopy" (Springer-Verlag, Berlin, 1985).
3. J. I. GOLDSTEIN, D. E. NEWBURY, P. ECHLIN, D. C. JOY, C. FIORI, A. D. ROMIG, JR, C. E. LYMAN and E. LIFSHIN, "Scanning Electron Microscopy and X-ray Microanalysis," 2nd edn. (Plenum Press, New York, 1992).
4. G. V. SARAPIN, "Electron Microscopy in Materials Science," edited by P. G. Merli and M. Vittori Antisari (World Scientific, Singapore, 1992) p. 547.
5. A. J. WILKINSON and P. B. HIRSCH, *Micron*. **28**(4) (1997) 279.
6. H. WATANABE and M. ICHIKAWA, *Rev. Sci. Instrum.* **67**(12) (1996) 4185.
7. K. Z. BABA-KISHI, *Scanning* **18** (1996) 315.
8. D. J. DINGLEY, K. Z. BABA-KISHI and V. RANDLE, "Atlas of Backscattering Kikuchi Diffraction Patterns," Series edited by B Cantor and M. J. Goringe (IOP Publishing, Bristal, 1995).
9. U. F. KNOCKS, C. N. TOME and H.-R. WENK, "Texture and Anisotropy" (Cambridge University Press, 1998) p. 167.
10. H. J. BUNGE, in Proc. XVII Conf. In Applied Crystallography, edited by H. Morawiec and Danuta Stroz (World Scientific, Singapore, 1998) p. 226.
11. D. J. DINGLEY, R. MACKENZIE and K. BABA-KISHI, in Proc. Microbeam Analysis, edited by P. E. Russell (San Francisco Press Inc., 1989) p. 435.
12. K. Z. BABA-KISHI, ULTRAMICROSCOPY **34** (1990) 205.
13. D. C. JOY, "Quantitative Scanning Electron Microscopy," edited by D. B. Holt, M. D. Muir, P. R. Grant and I. M. Boswarva (Academic Press London, N. Y., 1994) p. 131.
14. S. KIKUCHI, *Jap. J. Phys.* **5** (1928) 83.
15. K. SHINOHARA, *Phy. Rev.* **47** (1935) 730.
16. H. BOERSCH, *Physik. Z.* **38** (1937) 1000.
17. T. C. ISABELL and V. P. DRAVID, *Microscopy and Microanalysis* **III** (Supp.2) (1997) 557.
18. M. N. ALAM, M. BLACKMAN and D. W. PASHLEY, *Proc. Roy. Soc.* **A221** (1954) 224.
19. D. G. COATES, *Phil. Mag.* **16** (1967) 1179.
20. G. R. BOOKER, A. M. B. SHAW, M. J. WHELAN and P. B. HIRSCH, *ibid.* **16** (1967) 1185.
21. M. PITAVAL, P. MORIN, J. BOUDRY, E. VICARIO and G. FONTAINE, *Scanning Electron Microscopy* **1** (1977) 439.
22. J. T. CZERMUSZKA, N. J. LONG, E. D. BOYES and P. B. HIRSCH, *Phil. Mag. Lett.* **62**(4) (1990) 227.
23. H. NIEDRIG, *Scanning* **1** (1978) 17.
24. C. G. VAN ESSEN, E. M. SCHULSON and R. H. DONAGHAY, *Nature* **225** (1970) 847.
25. D. L. DAVIDSON, *Research and Development* **25** (1974) 34.
26. D. C. JOY and D. E. NEWBURY, *Scanning Electron Microscopy* **I** (1977) 445.
27. J. A. VENABLES and C. J. HARLAND, *Phil. Mag.* **27** (1973) 1193.
28. J. A. VENABLES, C. J. HARLAND and P. AKHTER, in Proc. 38th Annual Meeting EMSA, Claitors Press, Baton Rouge, 1980, p. 184.
29. J. A. VENABLES, C. J. HARLAND and R. BIN-JAYA, "Developments in Electron Microscopy and Analysis" (Academic Press, London, 1976) p. 101.
30. C. J. HARLAND, P. AKHTER and J. A. VENABLES, *J. Phys. E.* **14** (1981) 175.
31. B. W. BENNETT and A. W. PICKERING, *Scripta Met.* **18** (1984) 743.
32. A. R. PRESTON, M.Sc. Thesis, Bristol University (1983).
33. D. J. DINGLEY and N. RAZAVIZADEH, *Scanning Electron Microscopy* **IV** (1981) 287.
34. K. Z. BABA-KISHI and D. J. DINGLEY, *Scanning* **11**(6) (1989) 305.
35. D. J. DINGLEY and K. Z. BABA-KISHI, "Microscopy and Analysis," Issue 17 (AGC Publication, May 1990).
36. F. J. HUMPHREYS and M. FERRY, *Mater. Sci. Forum* **217** (1996) 529.
37. K. Z. BABA-KISHI, IX Conf. on Electron Microscopy of Solids, Krakow, Poland, May (1996) p. 191.
38. F. C. FRANK, *Less Common Metals* **28** (1972) 7.
39. D. B. WILLIAMS and C. B. CANTER, "Transmission Electron Microscopy" (Plenum Press N.Y., 1996) p. 291.
40. K. Z. BABA-KISHI, *J. Appl. Cryst.* **25** (1992) 737.
41. P. W. McCDONNELL, "Introduction to Map Projections," 2nd edn. (Landmark Enterprises, N.Y., 1991) p. 88.
42. H. HALBIG, P. L. RYDER and W. PITSCH, in Proc. 5th Cong. X-ray Optics and Microanalysis (Springer-Verlag, Berlin, 1969) p. 380.
43. S. BIGGIN and D. J. DINGLEY, *J. Appl. Cryst.* **10** (1977) 376.
44. J. A. VENABLES and R. BIN-JAYA, *Phil. Mag.* **35** (1977) 1317.
45. D. J. DINGLEY, *Scanning Electron Microscopy* **IV** (1981) 273.
46. D. J. DINGLEY and V. RANDLE, *J. Mater. Science* **27** (1992) 4545.
47. V. RANDLE, "Microtexture Determination and its Applications" (The Inst. Materials, Bourne Press, Bournemouth, 1992).
48. K. Z. BABA-KISHI, *Scanning* **20**(2) (1998) 1.

49. K. Z. BABA-KISHI and D. J. DINGLEY, *J. Appl. Cryst.* **22** (1989) 189.
50. D. J. DINGLEY and K. Z. BABA-KISHI, *Scanning Electron Microscopy* **2** (1986) 383.
51. K. Z. BABA-KISHI, *J. Appl. Cryst.* **24** (1991) 38.
52. *Idem.*, *Ultramicroscopy* **36** (1991) 355.
53. K. Z. TROOST, P. VAN DER SLUIS and D. J. GRAVESTEIN, *Appl. Phys. Lett.* **62** (1993) 1110.
54. A. J. WILKINSON, *Ultramicroscopy* **62** (1996) 237.
55. J. HJELEN and E. NES, in Proc. XIIth Int. Cong on Electron Microscopy (1990) p. 405.
56. R. A. SCHWARZER, *Microscopy and Analysis* **57** (Jan. 1997) 35.
57. O. FARSTAD, K. JOHANNESSEN and J. HJELEN, in Electron Microscopy, ICEM 14, Cancun (1998) p. 753.
58. T. PATTERSON, G. HEILBERG and J. HJELEN, in Electron Microscopy, ICEM 14, Symp. M, III, Cancun (1998) p. 775.
59. J. HUMPHREYS and I. BROUGH, HKL Technology Channel Users Meeting, Hobro, Denmark (1998) p. 17.
60. O. C. WELLS, "Scanning Electron Microscopy" (with contributions from A. Boyde, Eric Lifshin and Alex Rezanowich) (McGraw-Hill Book Company, NY, 1975).
61. *Idem.*, *Scanning* **2** (1979) 199.
62. O. C. WELLS, A. N. BROERS and C. G. BREMER, *Appl. Phys. Lett.* **23**(6) (1973) 353.
63. A. GOPINATH, "Quantitative Scanning Electron Microscopy," edited by Holt, Muir, Grant and Boswarva (Academic Press, London, NY, 1974).
64. T. YAMAMATO, *JEOL News* **15E**(3) (1977) 22.
65. J. T. L THONG, "Electron Beam Testing Technology," edited by John T. L. Thong (Plenum Press, NY, 1993).
66. P. B. HIRSCH, A HOWIE, R. B. NICHOLSON, D. W. PASHLEY and M. J. WHELAN, "Electron Microscopy of Thin Crystals" (Butterworth, London, 1965).
67. P. B. HIRSCH and C. J. HUMPHREYS, "Scanning Electron Microscopy," 3rd Conference (1977) p. 449.
68. L. REIMER, U. HEILERS and G. SALIGER, *Scanning* **8** (1986) 101.
69. R. SANDSTORM, J. P. SPENCER and C. J. HUMPHREYS, *J. Phys* D **7** (1974) 1030.
70. R. S. SHORTER and P. J. DOBSON, *ibid.* D **14** (1981) 59.
71. M. PITAVAL, "Microanalysis and Scanning Electron Microscopy," edited by L. Maurice, L. Meny and R. Tixier, Les Editions De Physique, BP 112-91402, Orsay, France (1979) p. 391.
72. P. B. HIRSCH and C. J. HUMPHREYS, Proc. 3rd Annual SEM Symp., edited by O. Johari (The ITT Research Inst., 1970) p. 449.
73. L. REIMER, H. G. BADDE, H. SEIDEL and W. BUHRING, *Z. Angew. Phys.* **31** (1971) 145.
74. E. VICARIO, M. PITAVAL and G. FONTAINE, Proc. 7th Int. Cong. on Electron Microscopy, edited by Favand. Grenoble, Vol. 2 (1970) p. 211.
75. J. P. SPENCER, C. J. HUMPHREYS and P. B. HIRSCH, *Phil. Mag.* **26** (1972) 192.
76. G. R. BOOKER, "Modern Diffraction and Imaging Techniques in Materials Science," edited by S. Amlinckx, R. Geners, J. Remant and J. Van Landuyt (North-Holland, London, 1970) p. 553.
77. C. R. HALL and P. B. HIRSCH, *Proc. Roy. Soc.* A **286** (1965) 158.
78. J. P. SPENCER and C. J. HUMPHREYS, Proc. 25th Anniversary Meeting of EMAG, IOP (1975) p. 310.
79. C. J. HUMPHREYS and P. B. HIRSCH, *Phil. Mag.* **18** (1968) 115.
80. P. PIROUZ and I. M. BOSWARVA, SEM Systems and Applications IOP. Conf. Ser. Vol. 18 (1973) p. 310.
81. S. L. DUDAREV, J. T. CZERNUSZKA, L. M. PENG, A. J. WILKINSON and M. J. WHELAN, Microsc. Semicond. Mater. Conf. IOP Conf. Ser. Vol. 146 (1995) p. 763.
82. S. L. DUDAREV, P. REZ and M. J. WHELAN, *Phys. Rev.* B **51**(6) (1995-II) 3397.
83. S. L. DUDAREV, J. AHMED, P. B. HIRSCH and A. J. WILKINSON, *Acta Crystallographica* A **55**(1) Part 2 (1999) 234.
84. L. REIMER, *Scanning* **2** (1979) 3.
85. C. S. HUNLBUT and C. KLEIN, "Manual of Mineralogy" 19th edn. (James Dana) (John Wiley, N.Y., 1971).
86. J. F. NYE, "Physical Properties of Crystals" (Oxford University Press, Clanendon, 1960).
87. G. BURNS and A. M. GLAZER, "Space Group for Solid State Scientists" (Academic Press, Boston, 1990).
88. C. HAMMOND, "The Basics of Crystallography and Diffraction" (Oxford Science Publications, 1997).
89. D. McKIE and C. McKIE, "Crystalline Solids" (Halsteal Press, J. Wiley, N.Y., 1974).
90. N. D. MEGAW, "Crystal Structures: A Working Approach" (W. B. Saunders Publishing Co., 1973).
91. L. BRAGG, G. F. CLARINGBULL and W. H. TAYLOR, "Crystal Structures of Minerals" (Bell Publishing, London, 1965).
92. E. W. NUFFIELD, "X-ray Diffraction Methods" (John Wiley, N.Y., 1966).
93. G. FRIEDEL, *C. R. Acad. Sci.* **157** Paris (1913) 1533.
94. S. HOSOYA and T. FUKAMACHI, *J. Appl. Cryst.* **6** (1973) 396.
95. P. GOODMAN and G. LEHEMPFUHL, *Acta. Cryst.* A **24** (1968) 339.
96. K. MARTHINSEN and R. HOIER, *ibid.* A **44** (1988a) 693.
97. *Idem.*, *ibid.* A **44** (1988b) 700.
98. S. R. HALL and J. M. STEWART, *ibid.* B **29** (1973) 579.
99. H. J. BUNGE, "Texture Analysis in Materials Science," Translated by P. R. Morris (Buttermonths, London, 1982).
100. H. R. WENK, "Preferred Orientation in Deformed Metals and Rocks." An Introduction to Modern Texture Analysis edited by H. R. Wenk (Academic Press, London, 1985).
101. D. JUN-JENSEN and N. H. SCHMIDT, "Recrystallization," edited by T. C. Chandra (Warrendale, P. A. TMS, 1990) p. 219.
102. S. I. WRIGHT, *J. Computer-Assited Microscopy* **5** (1993) 207.
103. B. L. ADAMS, S. I. WRIGHT and K. KUNZE, *Metallurgical Transactions A* **24A** (1993) 819.
104. T. A. MASON and B. L. ADAMS, *The Journal of Minerals. Metals and Materials Society* **46**(10) (1994) 43.
105. F. C. FRANK, *Metallurgical Transactions*, A The Metallurgical Society, The 1987 Institute of Metals Lecture, **19A** (1988) 403.
106. S. I. WRIGHT and D. J. DINGLEY, *Mater.Sci. Forum* **273-2** (1998) 209.
107. D. J. DINGLEY and D. P. FIELD, *Mater. Sci. Tech. Ser.* **13**(1) (1997) 69.
108. D. P. FIELD and D. J. DINGLEY, *J. Electron Mater.* **25**(11) (1996) 1767.
109. N. C. KRIEGER LASSEN, *Mater. Sci. Forum* **273–275** (1998) 201.
110. *Idem.*, *Mater. Sci. and Technology* **12** (1996) 837.
111. R. A. SCHWARZER, *MRS Symp. Proc.* **472** (1997) 118.
112. L. RYDE, Channel Users Meeting, HKL Technology, Hobo, Denmark, June 8–10 (1998) p. 45.
113. M. L. MULVIHILL, M. A. DUELGUEN, E. BISCHOFF and M. RUELE, *Z. Metallkd.* **89** (1998) 8.
114. D. J. DINGLEY, M. LONGDEN, J. WEINBREN and J. ALDERMAN, *Scanning Microscopy* **1**(2) (1987) 451.
115. V. RANDLE, *J. Microsc-Oxford* **195**, Part 3 (1999) 226.
116. R. K. DAVIES and V. RANDLE, *Mater. Sci. Tech. Ser.* **15**(9) (1999) 1015.
117. T. ZHAI, A. J. WILKINSON and J. W. MARTIN, *Mater. Sci. Forum* **331-3**, Part 1-3 (2000) 1549.
118. A. T. TUCKER, A. J. WILKINSON, M. B. HENDERSON, H. S. UBHI and J. W. MARTIN, *Materials Sci. and Technology* **16**(4) (2000) 427.
119. C. J. TAYLOR, T. ZHAI, A. J. WILKINSON and J. W. MARTIN, *Journal of Microscopy* (Oxford) **195**, Part 3 (1999) 239.
120. B. S. RHO, H. U. HONG and S. W. NAM, *Scripta Mater.* **43**(2) (2000) 167.
121. A. GODFREY and N. C. K. LASSEN, *J. Microscopy* (Oxford) **197**(3) (2000) 249.
122. C. BLOCHWITZ, J. BRECHBUHL and W. TIRSCHLER, *Mat. Sci. Eng-A-Instrut.* **210**(1/2) (1996) 42.
123. A. J. WILKINSON, *Inst. Phys. Conf. Ser.* **161** (1999) 115.
124. *Idem.*, *J. Electron Microsc.* **49**(2) (2000) 299.
125. D. P. FIELD, J. E. SANCHEZ, P. R. BESSER and D. J. DINGLEY, *J. Appl. Phys.* **82**(5) (1997) 2383.
126. D. P. FIELD, T. W. NELSON and D. J. DINGLEY, *Mater. Sci. Forum* **204**(1–2) (1996) 735.

127. S. GEIER, M. SCHRECK, R. HESSMER, B. RAUSCHENBACH, B. STRITZKER, K. KUNZE and B. L. ADAMS, *Appl. Phys. Lett.* **65**(14) (1994) 1781.
128. V. RANDLE, *Mat. Sci. Forum* **94–96** (1992) 233.
129. C. W. TAI and K. Z. BABA-KISHI, *Ferroelectrics* **241** (2000) 1.
130. D. CHATEIGNER, H.-R. WENK, A. PATEL, M. TODD and D. J. BARBER, *Integ. Ferroelectrics* **19** (1998) 121.
131. H. GARMESTANI and K. HARRIS, *Scripta Mater.* **41**(1) (1999) 47.
132. B. LEISS and D. J. BARBER, *TectonoPhysics* **303**(1–4) (1999) 51.
133. T. R. McNELLEY and M. E. McMAHON, *Supral 2004*, *Mater. Sci. Forum* **243** (1997) 527.
134. M. R. BACHE, W. J. EVANS and H. M. DAVIES, *J. Mater. Sci.* **32**(13) (1997) 3435.
135. A. F. NORMAN, I. BOROUGH and P. B. PRANGNELL, *Mater. Sci. Forum* **331-3**(1) (2000) 1713.
136. F. J. HUMPHREYS, P. S. BATE and P. J. HURLEY, *J. Microscopy* **201**(1) (2001) 50.
137. F. J. HUMPHREYS, *J. Mater. Sci.* **36** (2001) 3833.
138. P. N. QUESTED, P. J. HENDERSON and M. McLEAN, *Acta. Met. Mater.* **36** (1988) 2743.
139. R. A. D. MACKENZIE and D. J. DINGLEY, in Proc. XIth Int. Cong. on Electron Microscopy, *J. Elect. Microscopy Supplement* **35** (1986) 709.
140. R. STICKLER, C. W. HUGHES and G. R. BOOKER, *Scanning Electron Microscopy*, 4th Chicago Conf. (1971) p. 473.
141. A. J. WILKINSON and D. J. DINGLEY, *Acta. Metallurgica Materialia* **40** (1992) 3357.
142. A. J. WILKINSON, *Phil. Mag. Lett.* **73** (1996) 337.
143. J. AHMAD, A. J. WILKINSON and S. G. ROBERTS, *J. Microsc-Oxford* **195** Part 3 (1999) 239.
144. K. Z. BABA-KISHI and D. J. DINGLEY, *Inst. Phys. Conf. Ser.* No. **90** EMAG 97 (1987) 135.
145. J. R. MICHAEL and J. A. EADES, *Ultramicroscopy* **81** (2000) 67.
146. J. R. MICHAEL, *Microscopy and Microanalysis* **5** (1999) 218.

Received 5 December 2000
and accepted 14 November 2001